ARTICLE

Three-Dimensional Multiferroic Structures under Time-Harmonic Loading

Sonal Nirwal[1,3,*], Ernian Pan[1,2,*], Chih-Ping Lin[1,2] and Quoc Kinh Tran[1]

[1]Department of Civil Engineering, National Yang Ming Chiao Tung University, Hsinchu, 300, Taiwan

[2]Disaster Prevention and Water Environment Research Center, National Yang Ming Chiao Tung University, Hsinchu, 300, Taiwan

[3]Department of Applied Science, Krishna Institute of Engineering and Technology, Ghaziabad, 201206, India

*Corresponding Authors: Sonal Nirwal. Email: sonal.iitism@gmail.com; Ernian Pan. Email: ernian.pan@gmail.com

ABSTRACT

Magneto-electro-elastic (MEE) materials are a specific class of advanced smart materials that simultaneously manifest the coupling behavior under electric, magnetic, and mechanical loads. This unique combination of properties allows MEE materials to respond to mechanical, electric, and magnetic stimuli, making them versatile for various applications. This paper investigates the static and time-harmonic field solutions induced by the surface load in a three-dimensional (3D) multilayered transversely isotropic (TI) linear MEE layered solid. Green's functions corresponding to the applied uniform load (in both horizontal and vertical directions) are derived using the Fourier-Bessel series (FBS) system of vector functions. By virtue of this FBS method, two sets of first-order ordinary differential equations (i.e., N-type and LM-type) are obtained, with the expansion coefficients being Love numbers. It is noted that the LM-type system corresponds to the MEE-coupled P-, SV-, and Rayleigh waves, while the N-type corresponds to the purely elastic SH- and Love waves. By applying the continuity conditions across interfaces, the solutions for each layer of the structure (from the bottom to the top) are derived using the dual-variable and position (DVP) method. This method (i.e., DVP) is unconditionally stable when propagating solutions through different layers. Numerical examples illustrate the impact of load types, layering, and frequency on the response of the structure, as well as the accuracy and convergence of the proposed approach. The numerical results are useful in designing smart devices made of MEE solids, which are applicable to engineering fields like renewable energy.

KEYWORDS

Multiferroics; multilayers; Love numbers; Fourier-Bessel series; dual-variable and position method; time-harmonic

1 Introduction

In recent years, smart composite materials have found applications in ultrasonic imaging devices, space structures, and energy harvesting [1–4]. These smart materials are capable of altering their dimensions, shape, rigidity, and various mechanical properties when exposed to external temperature, electric field, mechanical field, and others.

Among the smart materials, multiferroic or magneto-electro-elastic (MEE) materials have energy conversion capacities [5]. While single-phase multiferroics have only weak magnetoelectric (ME) coupling, materials composed of piezoelectric (PE) and piezomagnetic (PM) phases can have strong

ME coupling for converting energy from one form into another [6–8]. Their capacity to convert and manipulate energies makes them useful in diverse fields. From innovative sensors capable of detecting subtle changes in magnetic (or electric) fields to actuators designed to respond dynamically to external stimuli, these materials become important in diverse engineering fields. Their role in developing advanced transducers, efficient energy harvesting systems, and even cutting-edge medical devices underscores their significance in shaping the future of technology and engineering [9–11]. Malleron et al. [12] conducted an experimental study on magnetoelectric transducers for powering small biomedical devices. Li et al. [13] investigated the static behaviour of MEE materials in a hygrothermal environment using the multi-physical cell-based smoothed finite element method (MCS-FEM). Their study highlights the significance of employing MCS-FEM for solving multi-physical problems. Sasmal et al. [14] reviewed recent progress in flexible magnetoelectric composites and devices for next-generation wearable electronics, focusing on strategic fabrication techniques to improve the performance of flexible ME composites and devices.

To fully exploit the potential of these advanced materials, it is essential to accurately model their behaviour under various conditions. One of the most effective tools for this purpose is the fundamental solution, also called Green's functions (GF). GFs are pivotal in various analytical and numerical techniques [15–17] as they provide a means to solve complex boundary-value problems involving different classes of materials such as MEE materials. Given the intricate coupling among magnetic, electric, and elastic fields in MEE solids, accurate determination and utilization of GFs become crucial. They help in understanding and predicting how these materials will respond to different stimuli, which is essential for designing applications [18–20]. For instance, in the development of advanced transducers and sensors, GFs enable precise calculations and optimizations necessary for high performance. This importance is particularly evident when smart materials are used in layered structures. The complexity of these structures requires precise solutions to boundary-value problems, which GFs can provide. Yang et al. [21] investigated the natural characteristics of anisotropic MEE multilayered plates using the analytical and finite element approach and drew their conclusion on three-layered plates with four different stacking sequences. Guided wave propagation in a multilayered MEE curved panel by the Chebyshev spectral elements method was discussed by Xiao et al. [22]. Vattree et al. [23] studied the semicoherent heterophase interfaces in 3D MEE multilayered composites under external loads. The appropriate structural interface conditions and the corresponding complicated boundary-value problem were solved using the mathematically elegant and computationally powerful Stroh formalism combined with the Fourier transform and dual-variable and position method (DVP). Singularity-free theory and adaptive finite element computations of arbitrarily shaped dislocation loop dynamics in 3D heterogeneous material structures are described by Vattré et al. [24]. Small-scale thermal analysis of piezoelectric–piezomagnetic Functionally Graded (FG) microplates using modified strain gradient theory was carried out by Hung et al. [25]. Kiran [26] studied thermal and hygrothermal buckling characteristics of porous magneto-electro-elastic skewed plates using third-order shear deformation theory. Additionally, Lyu et al. [27] conducted nonlinear dynamic modelling of geometrically imperfect MEE nanobeams made of functionally graded materials. Nonlinear isogeometric analysis of magneto-electro-elastic porous nanoplates was done by Phung et al. [28]. Circular loadings on the surface of an anisotropic and MEE half-space are investigated by Wang et al. [29]. Here, an analytical solution for a uniform and an indentation-type load is derived, distinguishing important features associated with the considered loadings. The different features of fracture analysis in PE and MEE materials are analyzed by Bui et al. [30] and Kiran et al. [31]. Various analytical and numerical methods have been proposed for solving the related problems in multilayered structures over the past decades [32–35]. In these studies, different real-life challenges such as imperfections, cracks, dynamic loads, and other

factors are explored. These aspects are crucial when designing layered structures, as they significantly influence the performance and reliability of actual devices.

Previous studies have explored the essential nature of MEE multilayered structures. Although these investigations can extract the most essential nature of MEE multilayered structures, they were mostly limited to the static response under vertical loading, employing relatively complicated methods. However, the dynamic responses and real-world applications necessitate more sophisticated approaches, which GFs can facilitate. Understanding the dynamic behavior of MEE multilayered structures is crucial for their integration into modern technological systems. The ability to accurately predict and control their performance under various operational conditions can significantly improve the design and functionality of smart devices. GFs, with their advanced capabilities, provide a robust framework for modelling and analyzing these complex interactions.

In this paper, we analyze the time-harmonic response of 3D multilayered transversely isotropic (TI) MEE layered solids induced by arbitrary time-harmonic loads in both horizontal and vertical directions (including the electric load). While previous studies have primarily focused on the static response, understanding the time-harmonic response is important for many applications that involve dynamic and oscillatory loading conditions [36]. Time-harmonic loads are particularly important because they simulate real-world conditions where the materials are subjected to time-dependent forces, such as in ultrasonic imaging, vibration control, and energy harvesting systems [37]. Computing the time-harmonic response allows for the accurate prediction of transient behaviors and the dynamic interaction between magnetic, electric, and mechanical fields within MEE materials, which is vital for optimizing the performance and efficiency of devices.

Recent advancements in the fundamental solutions for layered structures, including the Fourier-Bessel series (FBS) vector function [38] and the DVP method [16], enhance the analytical precision in the study of MEE materials. The FBS and DVP methods exhibit computational efficiency and robustness, making them particularly advantageous for addressing complex dynamic problems. These methods facilitate the accurate modelling and analysis of transient behaviors in multilayered structures. The FBS system of vector function is attractive, with the decoupled solutions (LM- and N-type) in each layer being simply expressed by the eigenvalues and eigenvectors. Additionally, the DVP method is effective for handling layering due to its stability and efficiency. Furthermore, in terms of the FBS system, the solved coefficients are discrete Love numbers [39], which can be saved and repeatedly used on the surface of the layered solid. Since the GFs are just the summation of the Love numbers (multiplied by the given base functions), they can be accurately and fast calculated. In this paper, the GFs corresponding to the surface loading over a circular area will be derived in detail, with numerical examples showing the influence of loading types, frequencies and layering on the solutions.

The results of this study have applications in several engineering fields. Specifically, understanding the time-harmonic responses of MEE materials can significantly enhance the design and performance of devices subjected to dynamic and oscillatory loading conditions. For example, accurate modelling of time-harmonic responses in ultrasonic imaging can lead to better image resolution and deeper tissue penetration. In vibration control, improved response predictions can enhance the stability and effectiveness of damping systems. In energy harvesting systems, the ability to predict and optimize the dynamic interaction between different fields can lead to more efficient energy conversion and storage solutions. By addressing these practical applications, this research contributes to the advancement of smart material technologies and their integration into various high-performance engineering systems.

2 Statement of the Problem

Fig. 1 depicts the 3D structure, which consists of an n-layered solid made of transversally isotropic (TI) -MEE solid materials. The Cartesian coordinate system (x, y, z) is attached to its (x, y)-plane on the surface and the layered solid in the positive z-direction. Each layer is ordered downward, with Layer 1 on the top (with $z_0 = 0$). Layer j is bounded by two interfaces, $z = z_{j-1}$ and $z = z_j$, with thickness $h_j = z_j - z_{j-1}$ ($j = 1, ..., n$). The last interface of Layer n, i.e., z_n, rests on the homogeneous MEE half-space. We assume that the adjacent layers are perfectly bonded, and that the uniform time-harmonic loads in both vertical and horizontal directions are applied on the surface of the structure within a circular region of radius a (see Fig. 1). Since the loads are proportional to $e^{i\omega t}$ where $\omega = 2\pi f$ in Hz $= 1/s$ is the angular frequency, the factor $e^{i\omega t}$ in the response will be omitted.
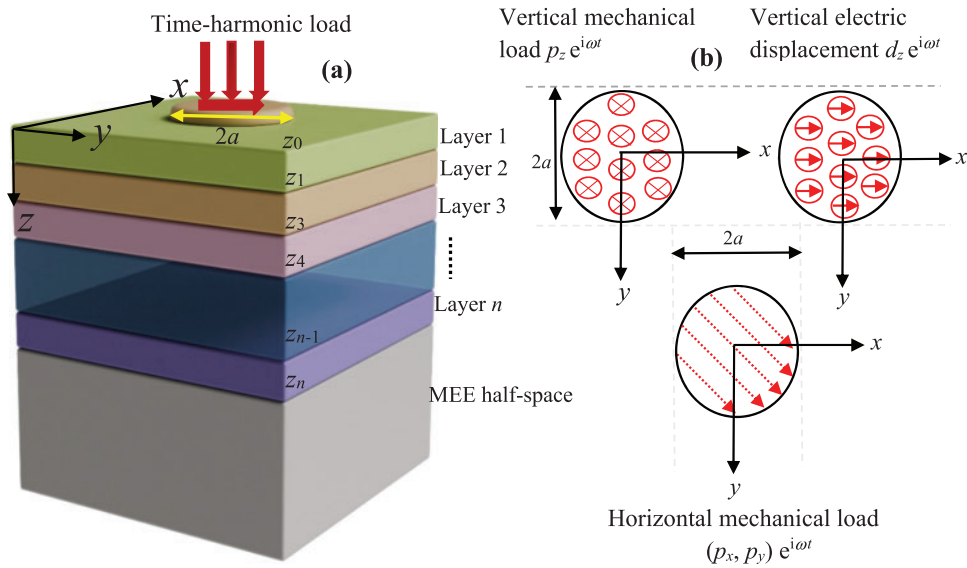

Figure 1: Schematic of the 3D structure composed of TI-MEE layered solid subjected to time-harmonic loads on its surface in (a), three types of time-harmonic loads, i.e., vertical mechanical load p_z, vertical electric displacement d_z and horizontal mechanical load (p_x, p_y) applied on the surface plane (x, y) of the structure within the circle of radius a in (b)

2.1 Governing Equations

The problem presented above can be solved in terms of either Cartesian or cylindrical coordinate systems. Here, we employ the FBS vector system to solve the problem. Thus, the equations of motion and the Gauss law in the MEE solid without body forces, electric charge, and magnetic monopoles (proportional to $e^{i\omega t}$) are given by [20]

$$\frac{\partial \sigma_{rr}}{\partial r} + \frac{1}{r}\frac{\partial \sigma_{r\theta}}{\partial \theta} + \frac{\partial \sigma_{rz}}{\partial z} + \frac{\sigma_r - \sigma_\theta}{2} + \rho\omega^2 u_r = 0$$

$$\frac{\partial \sigma_{r\theta}}{\partial r} + \frac{1}{r}\frac{\partial \sigma_{\theta\theta}}{\partial \theta} + \frac{\partial \sigma_{\theta z}}{\partial z} + \frac{2\sigma_{r\theta}}{r} + \rho\omega^2 u_\theta = 0$$

$$\frac{\partial \sigma_{rz}}{\partial r} + \frac{1}{r}\frac{\partial \sigma_{\theta z}}{\partial \theta} + \frac{\partial \sigma_{zz}}{\partial z} + \frac{\sigma_{rz}}{r} + \rho\omega^2 u_z = 0$$

$$\frac{\partial D_r}{\partial r} + \frac{1}{r}\frac{\partial D_\theta}{\partial \theta} + \frac{\partial D_z}{\partial z} + \frac{D_r}{r} = 0$$

$$\frac{\partial B_r}{\partial r} + \frac{1}{r}\frac{\partial B_\theta}{\partial \theta} + \frac{\partial B_z}{\partial z} + \frac{B_r}{r} = 0 \tag{1}$$

where σ_{ij} (N/m^2) ($i, j = r, \theta, z$) is mechanical stresses, D_j (C/m^2) is electric displacement, and B_j (T = Wb/m^2) is magnetic inductions; ρ (kg/m^3) and u_i (m) are mass density and elastic displacements.

The constitutive relation for TI-MEE materials (with its symmetry axis along z-axis) is given by [40]

$$\sigma_{rr} = c_{11}\gamma_{rr} + c_{12}\gamma_{\theta\theta} + c_{13}\gamma_{zz} - e_{31}E_z - q_{31}H_z$$

$$\sigma_{\theta\theta} = c_{12}\gamma_{rr} + c_{11}\gamma_{\theta\theta} + c_{13}\gamma_{zz} - e_{31}E_z - q_{31}H_z$$

$$\sigma_{zz} = c_{13}\gamma_{rr} + c_{13}\gamma_{\theta\theta} + c_{33}\gamma_{zz} - e_{33}E_z - q_{33}H_z$$

$$\sigma_{rz} = 2c_{44}\gamma_{rz} - e_{15}E_r - q_{15}H_\theta$$

$$\sigma_{\theta z} = 2c_{44}\gamma_{\theta z} - e_{15}E_\theta - q_{15}H_r$$

$$\sigma_{r\theta} = 2c_{66}\gamma_{r\theta}$$

$$D_r = 2e_{15}\gamma_{rz} + \eta_{11}E_r + d_{11}H_r$$

$$D_\theta = 2e_{15}\gamma_{\theta z} + \eta_{11}E_\theta + d_{11}H_\theta$$

$$D_z = e_{31}\gamma_{rr} + e_{31}\gamma_{\theta\theta} + e_{33}\gamma_{zz} + \eta_{33}E_z + d_{33}H_z$$

$$B_r = e_{15}\gamma_{rz} + \eta_{11}E_r + \mu_{11}H_r$$

$$B_\theta = e_{15}\gamma_{\theta z} + \eta_{11}E_\theta + \mu_{11}H_\theta$$

$$B_z = e_{31}\gamma_{rr} + e_{31}\gamma_{\theta\theta} + e_{33}\gamma_{zz} + \eta_{33}E_z + \mu_{33}H_z \tag{2}$$

where c_{ij} (N/m^2), e_{ij} (C/m^2), and ε_{ij} (C^2/N.m^2) are the elastic moduli, PE tensor, and dielectric permittivity tensor, respectively; q_{ij} (N/A.m), d_{ij} (C/A.m), and μ_{ij} (C^2/N.m^2) are the PM tensor, ME tensor and magnetic permeability tensor, respectively; γ_{ij} (dimensionless), E_i (V/m) and H_i (A/m) are the strain tensor, electric field and magnetic field.

The strain components γ_{ij}, electric field E_j and magnetic field H_j are related to the mechanical displacements u_i, electric potential ϕ (V) and magnetic potential ψ (A) by [40]

$$\gamma_{rr} = \frac{\partial u_r}{\partial r}, \ \gamma_{\theta\theta} = \frac{\partial u_\theta}{r\partial r} + \frac{u_r}{r}, \ \gamma_{zz} = \frac{\partial u_z}{\partial z}, \ \gamma_{\theta z} = \frac{1}{2}\left(\frac{\partial u_\theta}{\partial z} + \frac{\partial u_z}{r\partial z}\right)$$

$$\gamma_{rz} = \frac{1}{2}\left(\frac{\partial u_z}{\partial r} + \frac{\partial u_r}{\partial z}\right), \gamma_{r\theta} = \frac{1}{2}\left(\frac{\partial u_r}{r\partial\theta} + \frac{\partial u_\theta}{\partial r} - \frac{u_\theta}{r}\right)$$

$$E_r = -\frac{\partial\phi}{\partial r}, \ E_\theta = -\frac{1}{r}\frac{\partial\phi}{\partial\theta}, \ E_z = -\frac{\partial\phi}{\partial z}$$

$$H_r = -\frac{\partial\psi}{\partial r}, \ H_\theta = -\frac{1}{r}\frac{\partial\psi}{\partial\theta}, \ H_z = -\frac{\partial\psi}{\partial z} \tag{3}$$

2.2 Continuity Condition on any Interface $z = z_k$ (Except for the Last Half-Space)

Since we have considered that the internal interfaces between layers are perfectly bonded, the mechanical displacements, electric potential, magnetic potential, tractions, electric displacements, and magnetic induction are continuous across it (e.g., at $z = z_k$). Namely, we have

$$u_i(r, \theta, z_{k+}) = u_i(r, \theta, z_{k-}), \quad i = r, \theta, z$$

$$\phi(r, \theta, z_{k+}) = \phi(r, \theta, z_{k-})$$

$$\psi(r, \theta, z_{k+}) = \psi(r, \theta, z_{k-})$$

$$\sigma_{iz}(r, \theta, z_{k+}) = \sigma_{iz}(r, \theta, z_{k-})$$

$$D_z(r, \theta, z_{k+}) = D_z(r, \theta, z_{k-})$$

$$B_z(r, \theta, z_{k+}) = B_z(r, \theta, z_{k-}) \tag{4}$$

In the last homogeneous TI-MEE half-space, it is required that the solution remains finite.

2.3 Fundamental Solution in Terms of FBS System and DVP Method

2.3.1 FBS System of Vector Functions

To find the solution to the aforementioned boundary-value problem, the Fourier-Bessel series (FBS) vector functions are introduced [38]

$$\boldsymbol{L}(r, \theta; \lambda_{mk}) = \boldsymbol{e}_z S(r, \theta; \lambda_{mk})$$

$$\boldsymbol{M}(r, \theta; \lambda_{mk}) = \nabla S = \left(\partial_r \boldsymbol{e}_r + r^{-1}\partial_\theta \boldsymbol{e}_\theta\right) S$$

$$\boldsymbol{N}(r, \theta; \lambda_{mk}) = \nabla \times (S\boldsymbol{e}_z) = \left(r^{-1}\partial_\theta \boldsymbol{e}_r - \partial_r \boldsymbol{e}_\theta\right) S \tag{5}$$

where $\boldsymbol{e}_r$, $\boldsymbol{e}_\theta$ and $\boldsymbol{e}_z$ are the unit vectors along r-, θ-, and z-directions of the cylindrical system; λ_{mk} is the k-th zero of the Bessel function of order m, scaled by a large value R, i.e., $J_m(\lambda_{mk}R) = 0$ with deformation vanishes when $r > R$. Notice that the vector systems $\boldsymbol{L}$, $\boldsymbol{M}$ and $\boldsymbol{N}$ are orthogonal.

The scalar function in Eq. (5) is defined by

$$S(r, \theta; \lambda_{mk}) = J_m(\lambda_{mk}r)\, e^{im\theta}/\sqrt{2\pi}; \quad m = 0, \pm 1, \pm 2, \ldots \tag{6}$$

which satisfies the following Helmholtz equation:

$$\frac{\partial^2 S}{\partial r^2} + \frac{\partial S}{r\partial r} + \frac{\partial^2 S}{r^2\partial\theta^2} + \lambda_{mk}^2 S = 0 \tag{7}$$

Due to the orthogonal property of the FBS system (i.e., Eq. (5)), $\boldsymbol{u}$, ϕ and ψ can be expanded as [38]

$$\boldsymbol{u}(r, \theta, z) = u_r \boldsymbol{e}_r + u_\theta \boldsymbol{e}_\theta + u_z \boldsymbol{e}_z = \sum_m \sum_k [U_L(m, k; z)\,\boldsymbol{L}(r, \theta; \lambda_{mk}) + U_M(m, k; z)\,\boldsymbol{M}(r, \theta; \lambda_{mk})$$

$$+ U_N(m, k; z)\,\boldsymbol{N}(r, \theta; \lambda_{mk})] \tag{8}$$

$$\phi(r, \theta, z) = \sum_m \sum_k \Phi(z)\, S(r, \theta; \lambda_{mk}) \tag{9}$$

$$\psi(r, \theta, z) = \sum_m \sum_k \Psi(z)\, S(r, \theta; \lambda_{mk}) \tag{10}$$

Also, t (at $z =$ constant plane), $\boldsymbol{D}$ and $\boldsymbol{B}$ can be expanded as [38]

$$\boldsymbol{t}\,(r,\,\theta,\,z) = \sigma_{rz}\boldsymbol{e}_r + \sigma_{\theta z}\boldsymbol{e}_\theta + \sigma_{zz}\boldsymbol{e}_z$$

$$= \sum_m \sum_k [T_L\,(m,\,k;\,z)\,\boldsymbol{L}\,(r,\,\theta;\,\lambda_{mk}) + T_M\,(m,\,k;\,z)\,\boldsymbol{M}\,(r,\,\theta;\,\lambda_{mk})$$

$$+ T_N\,(m,\,k;\,z)\,\boldsymbol{N}\,(r,\,\theta;\,\lambda_{mk})] \tag{11}$$

$$\boldsymbol{D}\,(r,\,\theta,\,z) = D_r\boldsymbol{e}_r + D_\theta\boldsymbol{e}_\theta + D_z\boldsymbol{e}_z$$

$$= \sum_m \sum_k [D_L\,(m,\,k;\,z)\,\boldsymbol{L}\,(r,\,\theta;\,\lambda_{mk}) + D_M\,(m,\,k;\,z)\,\boldsymbol{M}\,(r,\,\theta;\,\lambda_{mk})$$

$$+ D_N\,(m,\,k;\,z)\,\boldsymbol{N}\,(r,\,\theta;\,\lambda_{mk})] \tag{12}$$

$$\boldsymbol{B}\,(r,\,\theta,\,z) = B_r\boldsymbol{e}_r + B_\theta\boldsymbol{e}_\theta + B_z\boldsymbol{e}_z$$

$$= \sum_m \sum_k [B_L\,(m,\,k;\,z)\,\boldsymbol{L}\,(r,\,\theta;\,\lambda_{mk}) + B_M\,(m,\,k;\,z)\,\boldsymbol{M}\,(r,\,\theta;\,\lambda_{mk})$$

$$+ B_N\,(m,\,k;\,z)\,\boldsymbol{N}\,(r,\,\theta;\,\lambda_{mk})] \tag{13}$$

where U_m, Φ, Ψ, T_m, D_m, B_m ($m = L$, M and N) are the expansion coefficients. Notice that, upon determining these coefficients, the corresponding physical quantities can be obtained by taking the simple summation in Eqs. (8)–(13).

We now derive the ordinary differential equations for these expansion coefficients and their solutions. First, from the constitutive relations, we find

$$T_L = -\lambda^2 c_{13} U_M + c_{33} U_L' + e_{33}\Phi' + q_{33}\Psi'$$

$$T_M = c_{44}\left(U_L + U_M'\right) + e_{15}\Phi + q_{15}\Psi$$

$$T_N = c_{44} U_N' \tag{14}$$

$$D_L = -\lambda^2 e_{31} U_M + e_{33} U_L' - \eta_{33}\Phi' - d_{33}\Psi' \tag{15a}$$

$$D_M = e_{15} U + e_{15} U_M' - \eta_{11}\Phi - d_{11}\Psi \tag{15b}$$

$$D_N = e_{15} U_N' \tag{15c}$$

$$B_L = -\lambda^2 q_{31} U_M + q_{33} U_L' - d_{33}\Phi' - \mu_{33}\Psi' \tag{16a}$$

$$B_M = q_{15} U_L + q_{15} U_M' - d_{11}\Phi - \mu_{11}\Psi \tag{16b}$$

$$B_N = q_{15} U_N' \tag{16c}$$

where a prime represents the derivative of the variable with respect to z.

Eqs. (14), (15a) and (16a) contain 10 expansion coefficients (i.e., U_L, U_M, U_N, Φ, Ψ, T_L, T_M, T_N, D_L and B_L) and need to be combined with the following 3 relations (from Eqs. (1)–(3)) to solve them

$$(c_{44} + c_{13})\, U'_L - \lambda^2 c_{11} U_M + c_{44} U''_M + (e_{15} + e_{31})\, \Phi' + (q_{15} + q_{31})\, \Psi' + \rho \omega^2 U_M = 0$$

$$\left(\lambda^2 U_N c_{66} - c_{44} U''_N - \rho \omega^2 U_N\right) = 0$$

$$- \lambda^2 c_{44} \left(U_L + U'_M\right) - \lambda^2 c_{13} U'_M + c_{33} U''_L - \lambda^2 e_{15} \Phi + e_{33} \Phi'' - \lambda^2 q_{15} \Psi + q_{33} \Psi'' + \rho \omega^2 U_L = 0$$

$$e_{33} U''_L - \eta_{33} \Phi'' - d_{33} \Psi'' - \lambda^2 (e_{15} + e_{31})\, U'_M - \lambda^2 e_{15} U_L + \lambda^2 \eta_{11} \Phi + \lambda^2 d_{11} \Psi_L = 0$$

$$q_{33} U''_L - d_{33} \Phi'' - \mu_{33} \Psi'' - \lambda^2 (q_{15} + q_{31})\, U'_M - \lambda^2 q_{15} U_L + \lambda^2 d_{11} \Phi + \lambda^2 \mu_{11} \Psi = 0 \qquad (17)$$

Now Eqs. (14), (15a), (16a) and (17) contain a total of ten equations for the ten coefficients. They can be converted into a linear system of first-order differential equations. Furthermore, both the LM-type and N-type systems are decoupled, with the N-type being purely elastic, as listed below:

$$\frac{d}{dz} \begin{bmatrix} U_N \\ T_N/\lambda \end{bmatrix} = \lambda_{mk} \begin{bmatrix} 0 & 1/c_{44} \\ c_{66} - \rho \omega^2/\lambda_{mk}^2 & 0 \end{bmatrix} \begin{bmatrix} U_N \\ T_N/\lambda \end{bmatrix} \qquad (18)$$

$$\frac{d}{dz} \begin{bmatrix} \boldsymbol{U}_{LM}(z) \\ \boldsymbol{T}_{LM}(z) \end{bmatrix} = \lambda_{mk} \begin{bmatrix} \boldsymbol{R}_1^{-1} \boldsymbol{R}_2^T & \boldsymbol{R}_1^{-1} \\ -\boldsymbol{R}_2 \boldsymbol{R}_1^{-1} \boldsymbol{R}_2^T + \boldsymbol{R}_3 + \boldsymbol{R}_4 & -\boldsymbol{R}_2 \boldsymbol{R}_1^{-1} \end{bmatrix} \begin{bmatrix} \boldsymbol{U}_{LM}(z) \\ \boldsymbol{T}_{LM}(z) \end{bmatrix} \qquad (19)$$

where

$$\boldsymbol{U}(z) = \begin{bmatrix} U_L & \lambda_{mk} U_M & \Phi & \Psi \end{bmatrix}^T ;$$
$$\boldsymbol{T}(z) = \begin{bmatrix} T_L/\lambda_{mk} & T_M & D_L/\lambda_{mk} & B_L/\lambda_{mk} \end{bmatrix}^T$$

and

$$\boldsymbol{R}_1 = \begin{bmatrix} c_{33} & 0 & e_{33} & q_{33} \\ 0 & c_{44} & 0 & 0 \\ e_{33} & 0 & -\eta_{33} & -d_{33} \\ q_{33} & 0 & -d_{33} & -\mu_{33} \end{bmatrix}, \boldsymbol{R}_2 = \begin{bmatrix} 0 & -c_{44} & 0 & 0 \\ c_{13} & 0 & e_{31} & q_{31} \\ 0 & -e_{15} & 0 & 0 \\ 0 & -q_{15} & 0 & 0 \end{bmatrix},$$

$$\boldsymbol{R}_3 = \begin{bmatrix} c_{44} & 0 & e_{15} & q_{15} \\ 0 & c_{11} & 0 & 0 \\ e_{15} & 0 & -\eta_{11} & -d_{11} \\ q_{33} & 0 & -d_{11} & -\mu_{11} \end{bmatrix}, \boldsymbol{R}_4 = -\frac{\rho \omega^2}{\lambda_{mk}^2} \begin{bmatrix} 1 & 0 & 0 & 0 \\ 0 & 1 & 0 & 0 \\ 0 & 0 & 0 & 0 \\ 0 & 0 & 0 & 0 \end{bmatrix}$$

Furthermore, the N-type solution is zero if the applied load is axis-symmetric.

2.3.2 Layer Solution

Solutions of Eqs. (18) and (19) can be simply expressed in terms of their eigenvalues and eigenvectors. The general solution in any layer, say in Layer j bounded by z_{j-1} and z_j, i.e., $z_{j-1} \le z \le z_j$ ($1 \le j \le n$), can be found as below:

$$\begin{bmatrix} \lambda_{mk} U_N(z) \\ T_N(z) \end{bmatrix} = \begin{bmatrix} 1 & 1 \\ c_{44} s_N & -c_{44} s_N \end{bmatrix} \begin{bmatrix} e^{\lambda_{mk} s_N (z - z_j)} & 0 \\ 0 & e^{-\lambda_{mk} s_N (z - z_{j-1})} \end{bmatrix} \begin{bmatrix} c_{N+} \\ c_{N-} \end{bmatrix} \qquad (20)$$

where

$$s_N = \sqrt{\left(c_{66} - \rho \omega^2/\lambda_{mk}^2\right)/c_{44}}$$

has a positive real part.

$$\begin{bmatrix} \boldsymbol{U}_{LM}(z) \\ \boldsymbol{T}_{LM}(z) \end{bmatrix} = \begin{bmatrix} \boldsymbol{E}_{11} & \boldsymbol{E}_{12} \\ \boldsymbol{E}_{21} & \boldsymbol{E}_{22} \end{bmatrix} \begin{bmatrix} \left\langle e^{\lambda_{mk}s_{11}(z-z_j)} \right\rangle & \boldsymbol{0} \\ \boldsymbol{0} & \left\langle e^{\lambda_{mk}s_{22}(z-z_{j-1})} \right\rangle \end{bmatrix} \begin{bmatrix} c_+ \\ c_- \end{bmatrix} \tag{21}$$

where $[\boldsymbol{E}]$ is the eigenmatrix and

$$\left\langle e^{\lambda_{mk}s_{11}z} \right\rangle = diag\left[e^{\lambda_{mk}s_1 z} \quad e^{\lambda_{mk}s_2 z} \quad e^{\lambda_{mk}s_3 z} \quad e^{\lambda_{mk}s_4 z} \right]; \quad \left\langle e^{\lambda_{mk}s_{22}z} \right\rangle = diag\left[e^{\lambda_{mk}s_5 z} \quad e^{\lambda_{mk}s_6 z} \quad e^{\lambda_{mk}s_7 z} \quad e^{\lambda_{mk}s_8 z} \right]$$

with the first four eigenvalues (s_1–s_4) having positive real parts and the other four having negative real parts.

2.3.3 DVP Matrix Method

To find the solution in the multilayered TI-MEE solid, the DVP method is adopted. Thus, by following Pan et al. [38], we have the following layer relation:

$$\begin{bmatrix} \lambda_{mk}\boldsymbol{U}_N(z_{j-1}) \\ \boldsymbol{T}_N(z_j) \end{bmatrix} = \begin{bmatrix} N_{11}^j & N_{12}^j \\ N_{21}^j & N_{22}^j \end{bmatrix} \begin{bmatrix} \lambda_{mk}\boldsymbol{U}_N(z_j) \\ \boldsymbol{T}_N(z_{j-1}) \end{bmatrix}$$

$$\begin{bmatrix} \boldsymbol{U}_{LM}(z_{j-1}) \\ \boldsymbol{T}_{LM}(z_j) \end{bmatrix} = \begin{bmatrix} \boldsymbol{S}_{11}^j & \boldsymbol{S}_{12}^j \\ \boldsymbol{S}_{21}^j & \boldsymbol{S}_{22}^j \end{bmatrix} \begin{bmatrix} \boldsymbol{U}_{LM}(z_j) \\ \boldsymbol{T}_{LM}(z_{j-1}) \end{bmatrix} \tag{22}$$

where

$$\begin{bmatrix} N_{11}^j & N_{12}^j \\ N_{21}^j & N_{22}^j \end{bmatrix} = \begin{bmatrix} e^{-\lambda_{mk}s_N h_j} & 1 \\ s_N c_{44} & -s_N c_{44} e^{-\lambda_{mk}s_N h_j} \end{bmatrix} \begin{bmatrix} 1 & e^{-\lambda_{mk}s_N h_j} \\ s_N c_{44} e^{-\lambda_{mk}s_N h_j} & -s_N c_{44} \end{bmatrix}^{-1}$$

$$\begin{bmatrix} \boldsymbol{S}_{11}^j & \boldsymbol{S}_{12}^j \\ \boldsymbol{S}_{13}^j & \boldsymbol{S}_{14}^j \end{bmatrix} = \begin{bmatrix} \boldsymbol{E}_{11}\left\langle e^{-\lambda_{mk}s_1 h_j} \right\rangle & \boldsymbol{E}_{12} \\ \boldsymbol{E}_{21} & \boldsymbol{E}_{22}\left\langle e^{\lambda_{mk}s_2 h_j} \right\rangle \end{bmatrix} \begin{bmatrix} \boldsymbol{E}_{11} & \boldsymbol{E}_{12}\left\langle e^{\lambda_{mk}s_2 h_j} \right\rangle \\ \boldsymbol{E}_{21}\left\langle e^{-\lambda_{mk}s_1 h_j} \right\rangle & \boldsymbol{E}_{22} \end{bmatrix}^{-1}$$

In a similar manner, the expansion coefficients for Layer $j+1$ can be obtained. Thus, by assuming the continuity condition between the two adjacent layers (i.e., Eq. (4)), we can determine the recursive relation between Layer j and Layer $j+1$, which is given by

$$\begin{bmatrix} \lambda_{mk}\boldsymbol{U}_N(z_{j-1}) \\ \boldsymbol{T}_N(z_{j+1}) \end{bmatrix} = \left[\boldsymbol{N}^{j:j+1} \right] \begin{bmatrix} \lambda_{mk}\boldsymbol{U}_N(z_{j+1}) \\ \boldsymbol{T}_N(z_{j-1}) \end{bmatrix}$$

$$\begin{bmatrix} \boldsymbol{U}_{LM}(z_{j-1}) \\ \boldsymbol{T}_{LM}(z_{j+1}) \end{bmatrix} = \left[\boldsymbol{S}^{j:j+1} \right] \begin{bmatrix} \boldsymbol{U}_{LM}(z_{j+1}) \\ \boldsymbol{T}_{LM}(z_{j-1}) \end{bmatrix} \tag{23}$$

where

$$\left[\boldsymbol{N}^{j:j+1} \right] = \begin{bmatrix} N_{11}^j N_{11}^{j+1} + N_{11}^j N_{12}^{j+1} \left(1 - N_{21}^j N_{12}^{j+1}\right)^{-1} N_{21}^j N_{11}^{j+1} & N_{12}^j + N_{11}^j N_{12}^{j+1} \left(1 - N_{21}^j N_{12}^{j+1}\right)^{-1} N_{22}^j \\ N_{21}^{j+1} + N_{22}^{j+1} \left(1 - N_{21}^j N_{12}^{j+1}\right)^{-1} N_{21}^j N_{11}^{j+1} & N_{22}^{j+1} \left(1 - N_{21}^j N_{12}^{j+1}\right)^{-1} N_{22}^j \end{bmatrix}$$

$$\left[\boldsymbol{S}^{j:j+1} \right] = \begin{bmatrix} \boldsymbol{S}_{11}^j \boldsymbol{S}_{11}^{j+1} + \boldsymbol{S}_{11}^j \boldsymbol{S}_{12}^{j+1} \left(\boldsymbol{I} - \boldsymbol{S}_{21}^j \boldsymbol{S}_{12}^{j+1}\right)^{-1} \boldsymbol{S}_{21}^j \boldsymbol{S}_{11}^{j+1} & \boldsymbol{S}_{12}^j + \boldsymbol{S}_{11}^j \boldsymbol{S}_{12}^{j+1} \left(\boldsymbol{I} - \boldsymbol{S}_{21}^j \boldsymbol{S}_{12}^{j+1}\right)^{-1} \boldsymbol{S}_{22}^j \\ \boldsymbol{S}_{21}^{j+1} + \boldsymbol{S}_{22}^{j+1} \left(\boldsymbol{I} - \boldsymbol{S}_{21}^j \boldsymbol{S}_{12}^{j+1}\right)^{-1} \boldsymbol{S}_{21}^j \boldsymbol{S}_{11}^{j+1} & \boldsymbol{S}_{22}^{j+1} \left(\boldsymbol{I} - \boldsymbol{S}_{21}^j \boldsymbol{S}_{12}^{j+1}\right)^{-1} \boldsymbol{S}_{22}^j \end{bmatrix}$$

The recursive relation (i.e., Eq. (23)) can be repeatedly applied in structure as long as the interfaces between the layers are perfect.

2.3.4 Boundary Conditions on the Surface

The boundary condition at $z = z_0$ (Fig. 1) (in terms of the Cartesian coordinate system and proportional to $e^{i\omega t}$) is given by [38]

$$\sigma_{xz} = \begin{Bmatrix} p_x & r \le a \\ 0 & r > 0 \end{Bmatrix}, \sigma_{yz} = \begin{Bmatrix} p_y & r \le a \\ 0 & r > 0 \end{Bmatrix}, \sigma_{zz} = \begin{Bmatrix} p_z & r \le a \\ 0 & r > 0 \end{Bmatrix}, D_z = \begin{Bmatrix} d_z & r \le a \\ 0 & r > 0 \end{Bmatrix} \tag{24}$$

In terms of the FBS system, we have obtained the following coefficients due to the applied loads on the surface of the structure [38]

$$T_L(z_0) = \frac{\sqrt{2\pi} p_z J_1(\lambda_{0k} a) a}{\lambda_{0k} N_1}, \quad m = 0$$

$$D_L(z_0) = \frac{\sqrt{2\pi} d_z J_1(\lambda_{0k} a) a}{\lambda_{0k} N_1}, \quad m = 0$$

$$T_M(z_0) = \frac{\sqrt{\pi}}{2} \frac{a J_1(\lambda_{1k} a)}{N_2} (\pm p_x - i p_y), \quad m = \pm 1$$

$$T_N(z_0) = \frac{\sqrt{\pi}}{2} \frac{a J_1(\lambda_{1k} a)}{N_2} (-i p_x \mp p_y), \quad m = \pm 1 \tag{25}$$

We consider the following three cases separately one by one here.

Case 1: Uniform vertical load p_z. For this case, we have

$$\boldsymbol{T}_{LM}(z_0) = \begin{bmatrix} \dfrac{\sqrt{2\pi} p_z J_1(\lambda_{0k} a) a}{\lambda_{0k} N_1} & 0 & 0 & 0 \end{bmatrix}^t$$

Case 2: Uniform vertical electric displacement d_z. For this case, we have

$$\boldsymbol{T}_{LM}(z_0) = \begin{bmatrix} 0 & 0 & \dfrac{\sqrt{2\pi} d_z J_1(\lambda_{0k} a) a}{\lambda_{0k} N_1} & 0 \end{bmatrix}^t$$

Case 3: Uniform horizontal load (p_x, p_y) in both x- and y-directions. For this case, we have

$$\boldsymbol{T}_{LM}(z_0) = \begin{bmatrix} 0 & \dfrac{\sqrt{\pi}}{2} \dfrac{a J_1(\lambda_{1k} a)}{N_2} (\pm p_x - i p_y) & 0 & 0 \end{bmatrix}^t, \text{ for } m = \pm 1$$

2.3.5 Expansion Coefficients on the Surface

With the surface traction coefficients, we apply the recursive relation for propagating the expansion coefficients from the surface z_0 to the last layer interface z_n to obtain the following relations:

$$\begin{bmatrix} \lambda_{mk} U_N(z_0) \\ T_N(z_n) \end{bmatrix} = \begin{bmatrix} N_{11}^{j:n} & N_{12}^{j:n} \\ N_{21}^{j:n} & N_{22}^{j:n} \end{bmatrix} \begin{bmatrix} \lambda_{mk} U_N(z_n) \\ T_N(z_0) \end{bmatrix}$$

$$\begin{bmatrix} \boldsymbol{U}_{LM}(z_0) \\ \boldsymbol{T}_{LM}(z_n) \end{bmatrix} = \begin{bmatrix} \boldsymbol{S}_{11}^{j:n} & \boldsymbol{S}_{12}^{j:n} \\ \boldsymbol{S}_{21}^{j:n} & \boldsymbol{S}_{22}^{j:n} \end{bmatrix} \begin{bmatrix} \boldsymbol{U}_{LM}(z_n) \\ \boldsymbol{T}_{LM}(z_0) \end{bmatrix} \tag{26}$$

On the last interface $z = z_n$, the unknowns in Eq. (26) are related as

$$T_N(z_n) = \left[E_{22}(E_{12})^{-1}\right]U_N(z_n)$$

$$\boldsymbol{T}_{LM}(z_n) = \left[\boldsymbol{E}_{22}(\boldsymbol{E}_{12})^{-1}\right]\boldsymbol{U}_{LM}(z_n) \tag{27}$$

where E_{ij} ($\boldsymbol{E}_{ij}$) are the eigenvector elements (submatrices) in the last MEE half-space.

Combined with Eq. (27), we can solve, from Eq. (26), the coefficients of displacements, electric potential, and magnetic potential on the surface of the layered structure, as given below.

Due to the applied vertical load (i.e., $m = 0$), we have only LM-type system, for which the expansion coefficients on the surface is given by

$$\boldsymbol{U}_{LM}(z_0) = \left[\boldsymbol{S}_{11}^{j:n}\left(\boldsymbol{E}_{22}(\boldsymbol{E}_{12})^{-1} - \boldsymbol{S}_{21}^{j:n}\right)^{-1}\boldsymbol{S}_{22}^{j:n} + \boldsymbol{S}_{12}^{j:n}\right]\boldsymbol{T}_{LM(0)}(z_0) \tag{28}$$

where

$$\mathbf{T}_{LM}(z_0) = \left[\frac{\sqrt{2\pi}\,p_z J_1(\lambda_{0k}a)\,a}{\lambda_{0k}N_1} \quad 0 \quad 0 \quad 0\right]^t; \mathbf{T}_{LM}(z_0) = \left[0 \quad 0 \quad 0 \quad \frac{\sqrt{2\pi}\,d_z J_1(\lambda_{0k}a)\,a}{\lambda_{0k}N_1}\right]^t$$

for the vertical mechanical load and vertical electric displacement, respectively.

Due to the applied horizontal load (i.e., for $m = \pm 1$) we have both N-type and LM-type systems, and for those, the coefficients on the surface are given by

$$\{\lambda_{1k}U_N(z_0)\} = \left[N_{11}^{j:n}\left(E_{22}(E_{12})^{-1} - N_{21}^{j:n}\right)^{-1}N_{22}^{j:n} + N_{12}^{j:n}\right]T_{N(1)}(z_0)$$

$$\boldsymbol{U}_{LM}(z_0) = \left[\boldsymbol{S}_{11}^{j:n}\left(\boldsymbol{E}_{22}(\boldsymbol{E}_{12})^{-1} - \boldsymbol{S}_{21}^{j:n}\right)^{-1}\boldsymbol{S}_{22}^{j:n} + \boldsymbol{S}_{12}^{j:n}\right]\boldsymbol{T}_{LM(1)}(z_0) \tag{29}$$

and

$$\{\lambda_{1k}U_N(z_0)\} = \left[N_{11}^{j:n}\left(E_{22}(E_{12})^{-1} - N_{21}^{j:n}\right)^{-1}N_{22}^{j:n} + N_{12}^{j:n}\right]T_{N(-1)}(z_0)$$

$$\boldsymbol{U}_{LM}(z_0) = \left[\boldsymbol{S}_{11}^{j:n}\left(\boldsymbol{E}_{22}(\boldsymbol{E}_{12})^{-1} - \boldsymbol{S}_{21}^{j:n}\right)^{-1}\boldsymbol{S}_{22}^{j:n} + \boldsymbol{S}_{12}^{j:n}\right]\boldsymbol{T}_{LM(-1)}(z_0) \tag{30}$$

where

$$\boldsymbol{T}_{LM(1)}(z_0) = \left[0 \quad \frac{\sqrt{\pi}}{2}\frac{aJ_1(\lambda_{1k}a)}{N_2}(p_x - ip_y) \quad 0 \quad 0\right]^t$$

$$\boldsymbol{T}_{LM(-1)}(z_0) = \left[0 \quad \frac{\sqrt{\pi}}{2}\frac{aJ_1(\lambda_{1k}a)}{N_2}(-p_x - ip_y) \quad 0 \quad 0\right]^t$$

$$T_{N(1)}(z_0) = \frac{\sqrt{\pi}}{2}\frac{aJ_1(\lambda_{1k}a)}{N_2}(p_x - ip_y)$$

$$T_{N(-1)}(z_0) = \frac{\sqrt{\pi}}{2}\frac{aJ_1(\lambda_{1k}a)}{N_2}(-p_x - ip_y)$$

Once the coefficients on the surface are obtained, we can find the solution at any point on the surface of the structure by carrying out the summation (i.e., Eqs. (8)–(13)). To find the solutions at any specific z level, we just need to replace z_0 with z in Eq. (26). Since coefficients are discreet numbers, they represent the exact Love numbers [39]. These Love numbers are advantageous to simplify the

computation process, as they can be pre-calculated and stored for repeated use in calculating the GFs [41].

3 Numerical Studies

3.1 Validation and Convergence of the Problem

Before presenting numerical results, the present field solutions are validated against existing ones and found to be consistent with the solution reported by Pan et al. [38], Chu et al. [40] and Qi et al. [42]. Fig. 2 illustrates the accuracy of the current method as compared with those of Chu et al. [40] and Qi et al. [42].
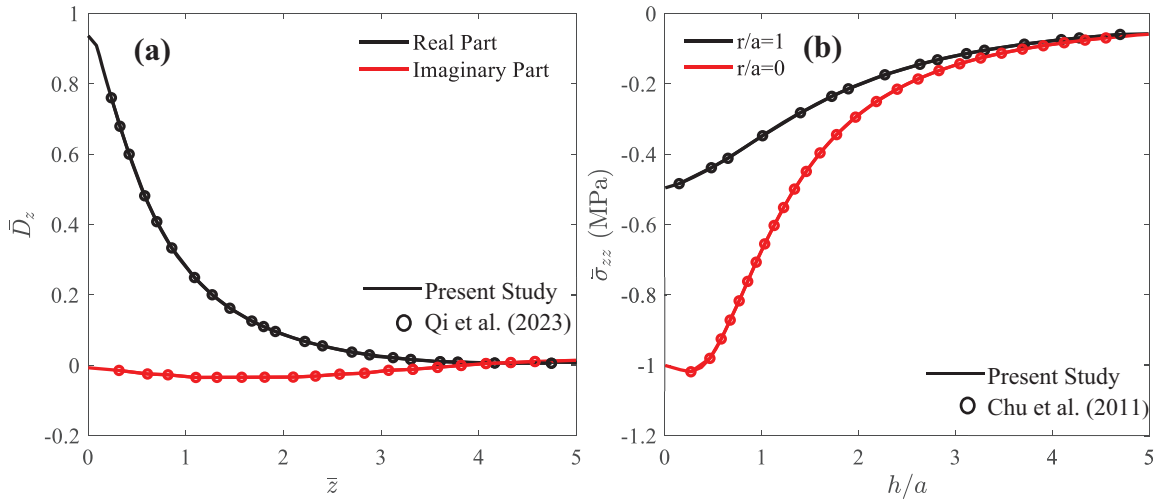

Figure 2: Variation of electric displacement $\overline{D}_z$ with respect to depth due to the electrical loading $\bar{d}_z$ ($= d_z/p_z$) on the surface of the half-space structure [42] (a), Variation of stress $\overline{\sigma}_{zz}$ with respect to the thickness of the surface layer due to applied mechanical load p_x on the surface of a two-layered structure for different field quantitates at the interface ($r/a = 0$ and $r/a = 1$) [40] (b)

A loading radius of $a = 1$ nm is located on the surface with its center at the origin of the coordinate system. In the calculation, a small material damping factor, i.e., $\beta = 0.0001$, is applied to the material. Namely, c_{kj}, e_{kj}, q_{kj}, η_{kj}, μ_{kj} and d_{kj} are replaced by $c_{kj}(1 + 2i\beta)$, $e_{kj}(1 + 2i\beta)$, $q_{kj}(1 + 2i\beta)$, $\eta_{kj}(1 + 2i\beta)$, $\mu_{kj}(1 + 2i\beta)$ and $d_{kj}(1 + 2i\beta)$ during the numerical computation. Furthermore, R in the FBS is fixed at 1500 nm (i.e., $R = 1500 a$) and $M = 9000$. In presenting the numerical findings in the paper, dimensionless parameters are used, as defined below.

$$\bar{x} = x/a; \ \bar{z} = z/a; \ \bar{a} = a/a; \ \bar{p}_x = p_x/c_{max}; \ \bar{d}_z = d_z/e_{max}; \ \bar{p}_z = p_z/c_{max}; \ \bar{u}_x = u_x/a; \ \bar{u}_z = u_z/a;$$
$$\bar{\phi} = \phi/\phi_{max}; \ \bar{\Psi} = \Psi/\Psi_{max}; \ \bar{\omega} = \omega a\sqrt{(\rho_{max}/c_{max})}; \ \bar{\sigma}_{zz} = \sigma_{zz}/c_{max}; \ \bar{D}_z = D_z/e_{max}; \ \bar{B}_z = B_z/q_{max}.$$

where c_{max}, e_{max}, and q_{max} are the maxima of the corresponding elastic, piezoelectric, piezomagnetic coefficients, and ρ_{max} the maximum density, and $\phi_{max} = e_{max}/a$ and $\psi_{max} = q_{max}/a$. The normalized electric and magnetic potentials are still dimensional variables.

Fig. 3 shows the surface displacements $\bar{u}_x$ and electric potential $\bar{\phi}$ induced by the horizontal mechanical load $\bar{p}_x$ for different truncation numbers M of the series (i.e., truncated at 10, 50, 100, 500, 1000). It is observed that, with increasing M, the solutions converge.

3.2 Time-Harmonic Loading on MEE Structures

Illustrative examples of the applied static and time-harmonic loads in nanoscale MEE multilayered structures are discussed in this section. The importance of layered structures in engineering lies in their capacity to offer tailored and multifunctional properties, making them pivotal in various applications. Understanding the dynamic behavior of MEE-layered structures and their distinct stacking configurations is essential for designing engineering structures with desired mechanical, electric, or magnetic characteristics, ensuring optimal performance in specific applications.
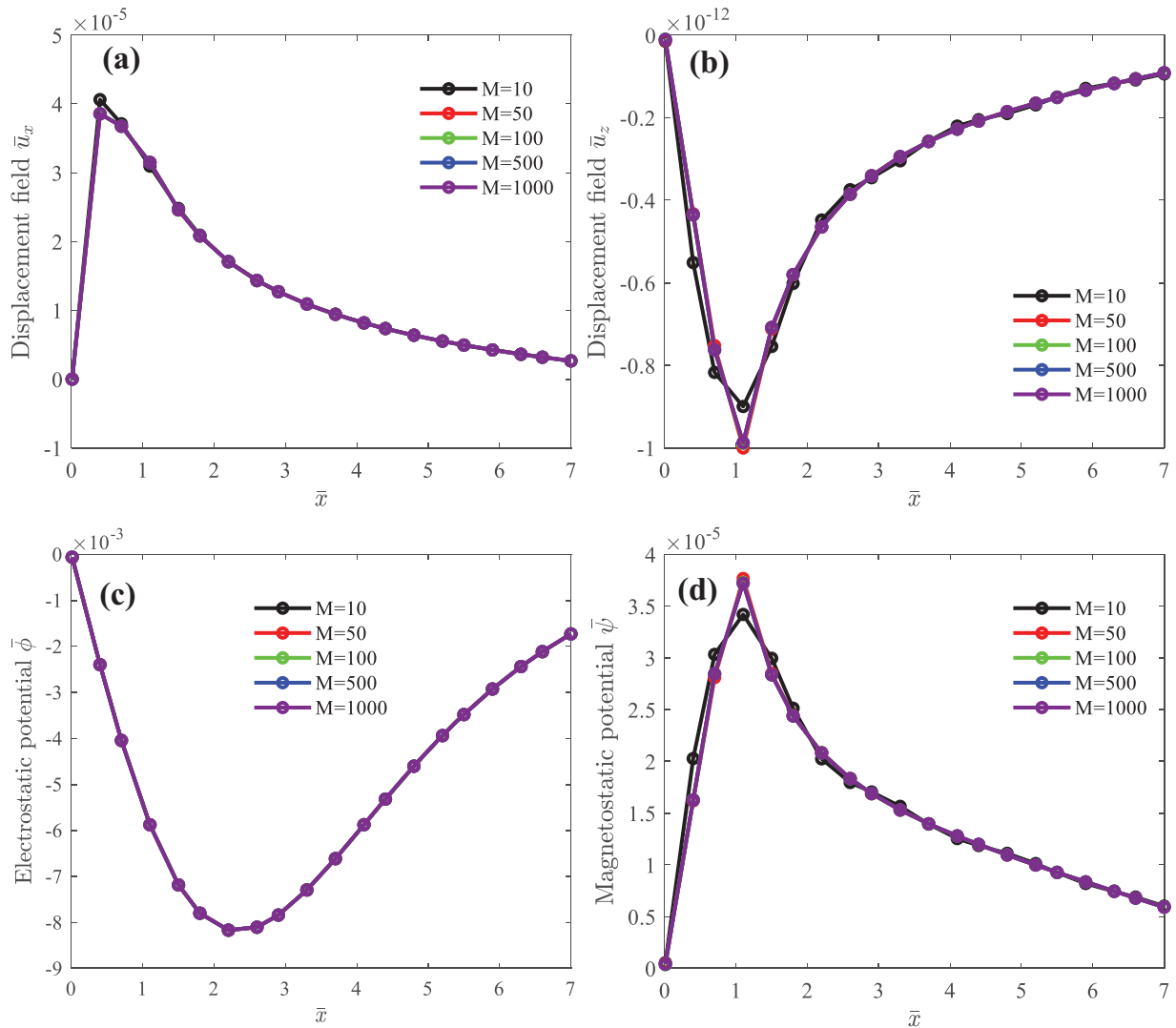
Figure 3: Surface elastic displacement $\bar{u}_x$ in (a), $\bar{u}_z$ in (b), electric potential $\bar{\phi}$ in (c), and magnetostatic potential $\bar{\psi}$ in (d) in a two-layered model (BaTiO$_3$/CoFe$_2$O$_4$) due to applied vertical mechanical load $\bar{p}_x$ on the surface, for truncation number $M = 10, 50, 100, 500$ and 1000)

The proposed framework is applied to analyze the impact of vibration frequency and different configurations in half-space, bi-layered, tri-layered, and multilayered media. The structures are made of CoFe$_2$O$_4$ (magnetostrictive cobalt ferrite, CFO) and BaTiO$_3$ (piezoelectric barium titanite, BTO),

and their composite, i.e., 0.25, 0.50 and 0.75 BTO for which the properties of the material are taken from Vattré et al. [24].

3.2.1 Under Vertical Mechanical Loading

The static and time-harmonic responses due to the circular vertical mechanical load $\bar{p}_z$ on different layered structures are shown in Figs. 4–7.
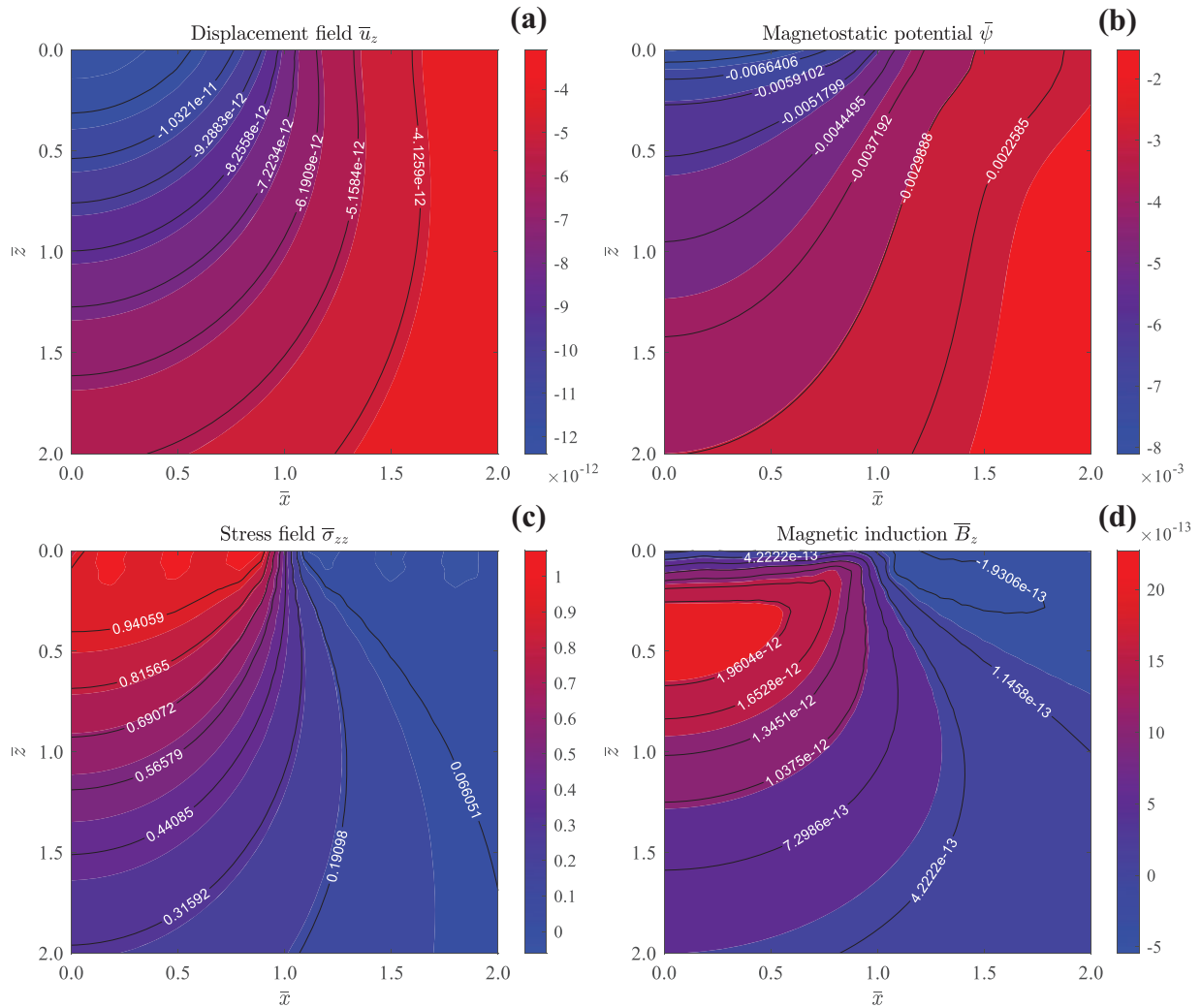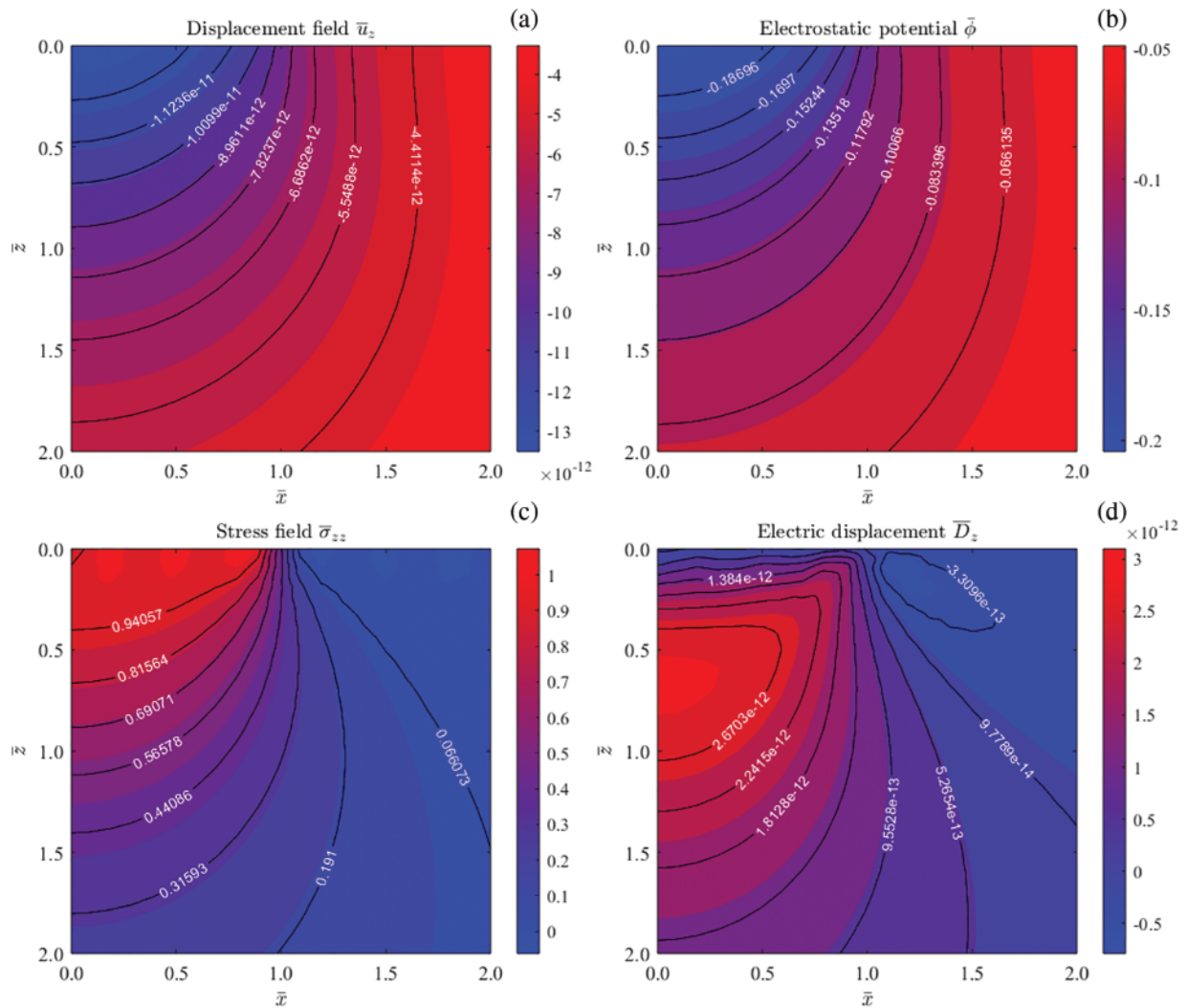

Figure 4: Contours of elastic displacement $\bar{u}_z$ in (a), magnetostatic potential $\bar{\psi}$ in (b), stress $\bar{\sigma}_{zz}$ in (c), and magnetic induction $\bar{B}_z$ in (d) in homogeneous CFO half-space due to applied vertical mechanical load $\bar{p}_z$ on the surface

Figure 5: Contours of elastic displacement $\overline{u}_z$ in (a), electrostatic potential $\overline{\phi}$ in (b), stress $\overline{\sigma}_{zz}$ in (c), and electric displacement $\overline{D}_z$ in (d) in homogeneous BTO half-space due to applied vertical mechanical load $\overline{p}_z$ on the surface
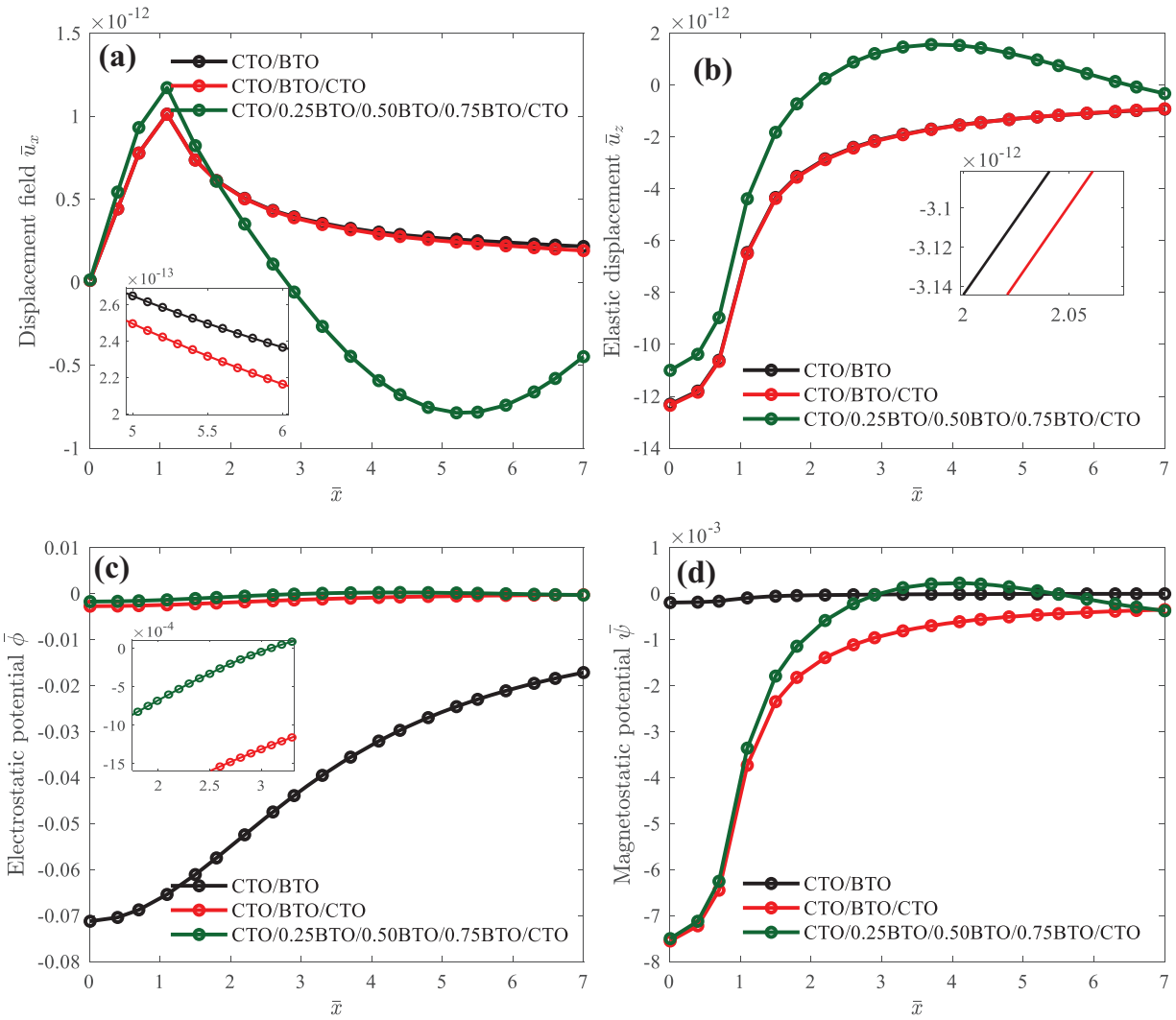
Figure 6: Elastic displacement $\bar{u}_x$ in (a), elastic displacement $\bar{u}_z$ in (b), electrostatic potential $\bar{\phi}$ in (c), magnetostatic potential $\bar{\psi}$ in (d) in three different layered models due to applied vertical mechanical load $\bar{p}_z$ on the surface
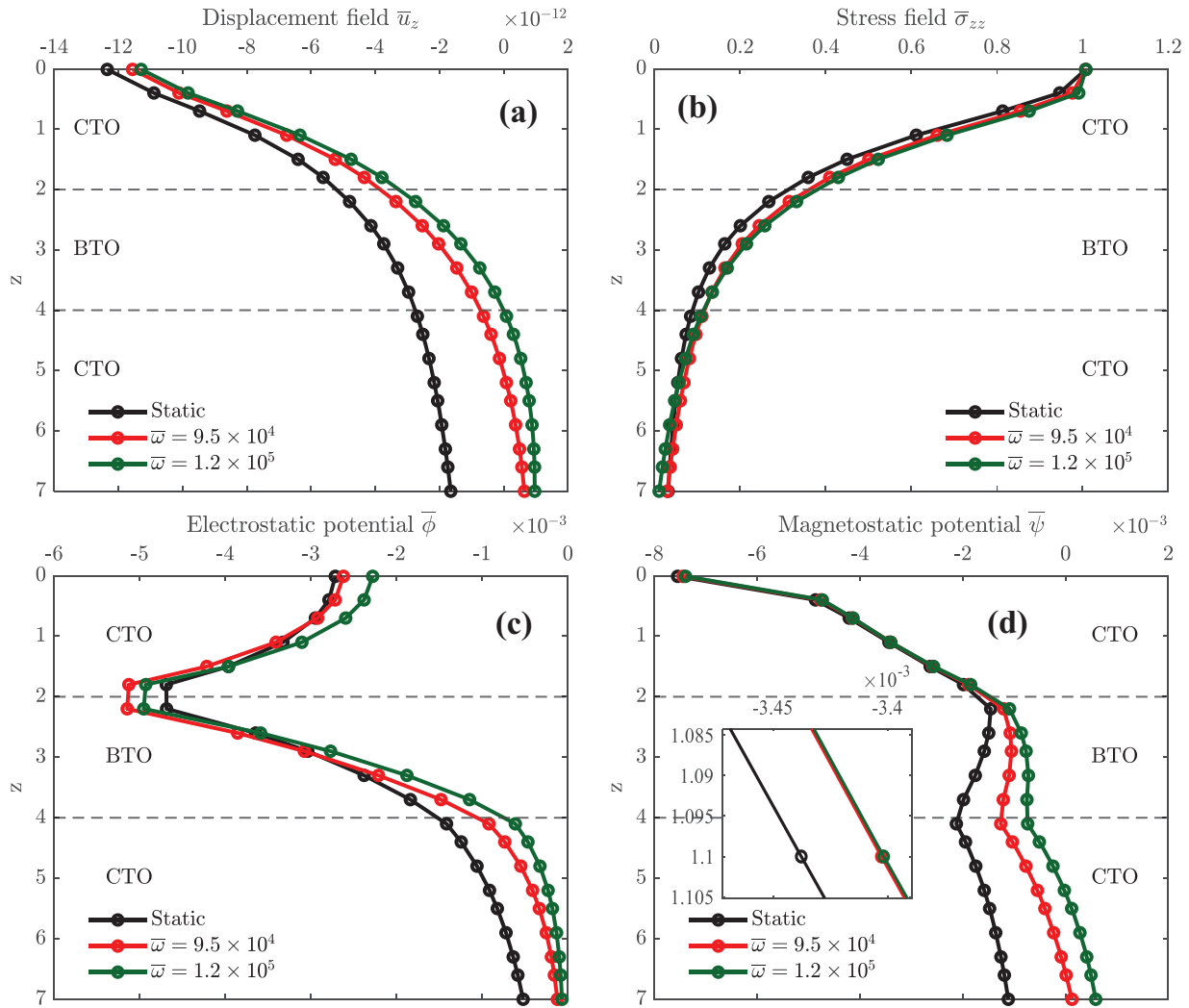
Figure 7: Effect of frequencies on elastic displacement $\bar{u}_x$ in (a), stress $\bar{\sigma}_{zz}$ in (b), electrostatic potential $\bar{\phi}$ in (c), and magnetostatic potential $\bar{\psi}$ in (d) in tri-layered CFO/BTO/CFO structure due to applied vertical mechanical load $\bar{p}_z$ on the surface

Fig. 4 presents the 2D contours of vertical elastic displacement $\bar{u}_z$, magnetic potential $\bar{\psi}$, stress $\bar{\sigma}_{zz}$, and magnetic induction $\bar{B}_z$ induced by a static vertical mechanical load (i.e., $\bar{\omega} = 0$) in a homogeneous CFO half-space. Field concentrations are clearly observed around the loading center. Similar features can be observed in Fig. 5 for the vertical elastic displacement $\bar{u}_z$, electrostatic potential $\bar{\phi}$, stress $\bar{\sigma}_{zz}$, and electric displacement $\bar{D}_z$ induced by the same static load (i.e., $\bar{\omega} = 0$) but in the homogeneous BTO half-space. It should be pointed out that while their variation patterns are similar, their magnitudes are different, particularly for the induced electrostatic potential and electric displacement in the two different half-spaces.

Fig. 6 illustrates the spatial distribution of field quantities on the surface, induced by the vertical mechanical load in CFO/BTO bi-layered, CFO/BTO/CFO tri-layered, and CFO/αBTO/CFO (α = 0.25, 0.50 and 0.75) multilayered structures. In Fig. 6a, it is noted that for $1 < \bar{x} < 2$, the magnitude

of the displacement field across all structures shows only minimal variation. However, for $\bar{x} > 2$, a significant difference among the different layups is observed. This feature can be further observed in Fig. 6b,d. These observations can be applied to the design of layered composites in flexible electronics, where precise control of displacement fields is critical.

Fig. 7 shows the distribution of elastic displacement $\bar{u}_z$, stress $\bar{\sigma}_{zz}$, electric field $\bar{\phi}$ and magnetic fields $\bar{\psi}$ along $\bar{z}$-axis for three different frequencies in tri-layered CFO/BTO/CFO. It can be observed that, with increasing frequency, the amplitude of most field quantities decreases. Also, due to the material property mismatch between the layers, the slopes of the electric potential $\bar{\phi}$ and magnetic potential $\bar{\psi}$ experience sharp discontinuities at the interface. These observations highlight the intricate interactions between frequency and material properties. Understanding how different frequencies affect the behaviour of materials can be applied to the design of electromechanical devices that operate under varying frequency conditions. This is crucial for the optimization of frequency-dependent devices such as sensors and resonators used in communication systems and medical equipment.

3.2.2 Under Vertical Electric Displacement

The static and time-harmonic responses due to the circular vertical electric displacement $\bar{d}_z$ on different layered structures are shown in Figs. 8–10.

Fig. 8 presents contours of elastic displacement $\bar{u}_z$, electric potential $\bar{\phi}$, stress $\bar{\sigma}_{zz}$, and $\overline{D}_z$ induced by a static load (i.e., $\bar{\omega} = 0$) in a homogeneous BTO half-space. It is observed that the contours of the elastic displacement and electric potential are similar to each other (Fig. 8a,b), but the stress and electric displacement show different variations (Fig. 8c,d).

Fig. 9 illustrates the spatial distribution of elastic displacements $\bar{u}_x$, elastic displacement $\bar{u}_z$, electric potential $\bar{\phi}$, and magnetic potential $\bar{\Psi}$ under applied electric displacement in the bi-layered, tri-layered, and multilayered structures. From Fig. 9a,b, it is observed that the amplitudes of displacements ($\bar{u}_x$ and $\bar{u}_z$,) in both tri-layered and multilayered structures are very close to each other, while those for bi-layered structures appear to be significantly different. As for the electric potential $\bar{\phi}$, its amplitude appears to remain largely unaffected (Fig. 9c).

Fig. 10 shows how different frequencies (i.e., $\bar{\omega} = 0$, 9.5×10^4 and 1.2×10^5) influence the distribution of elastic displacement $\bar{u}_z$, stress $\bar{\sigma}_{zz}$, electric field $\bar{\phi}$ and magnetic field $\bar{\psi}$ along the z-axis when the electric displacement $\bar{d}_z$ is applied on the surface of the tri-layered CFO/BTO/CFO solid. It is interesting to observe that while the electric potential is nearly insensitive to varying frequencies (Fig. 10c), other physical quantities are very different at different frequencies (Fig. 10a,b,d).
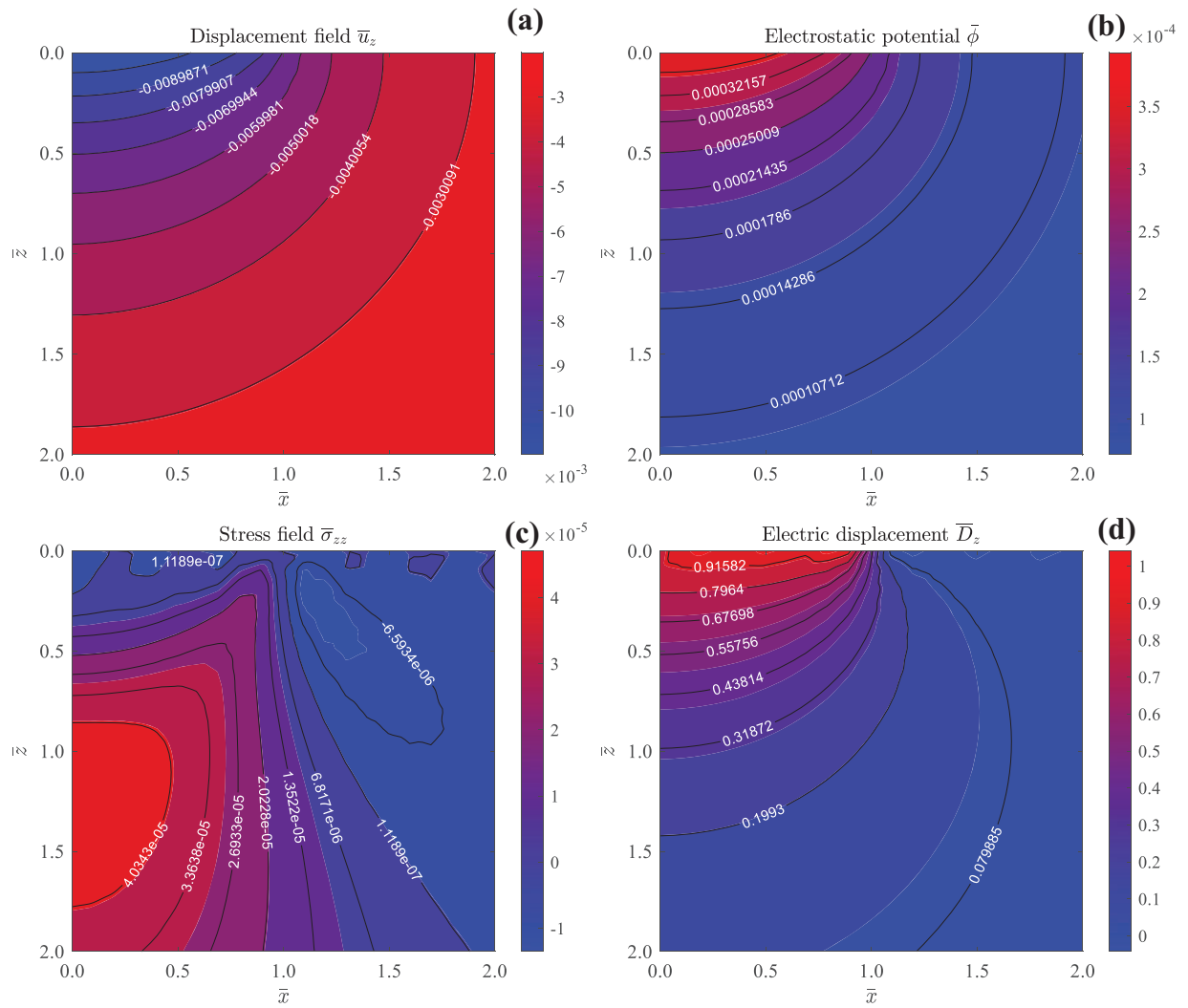
Figure 8: Contours of elastic displacement $\bar{u}_z$ in (a), electrostatic potential $\bar{\phi}$ in (b), stress $\bar{\sigma}_{zz}$ in (c), and electric displacement $\overline{D}_z$ in (d) in homogeneous BTO half-space due to applied vertical electric load $\bar{d}_z$ on the surface
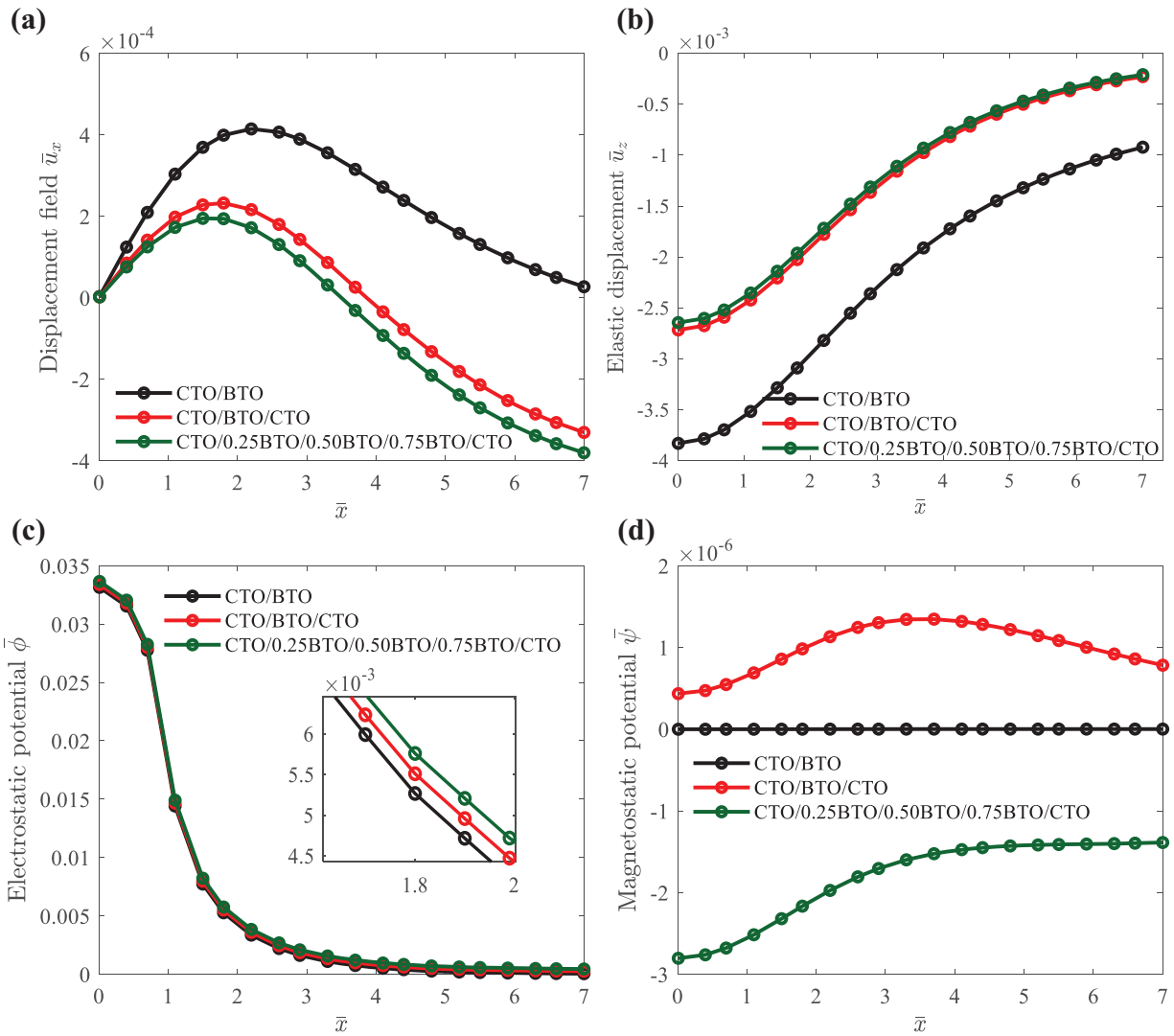
Figure 9: Surface elastic displacement $\bar{u}_x$ in (a), elastic displacement $\bar{u}_z$ in (b), electrostatic potential $\bar{\phi}$ in (c), magnetostatic potential $\bar{\psi}$ in (d) in three different layered models due to applied vertical electric displacement $\bar{d}_z$ on the surface
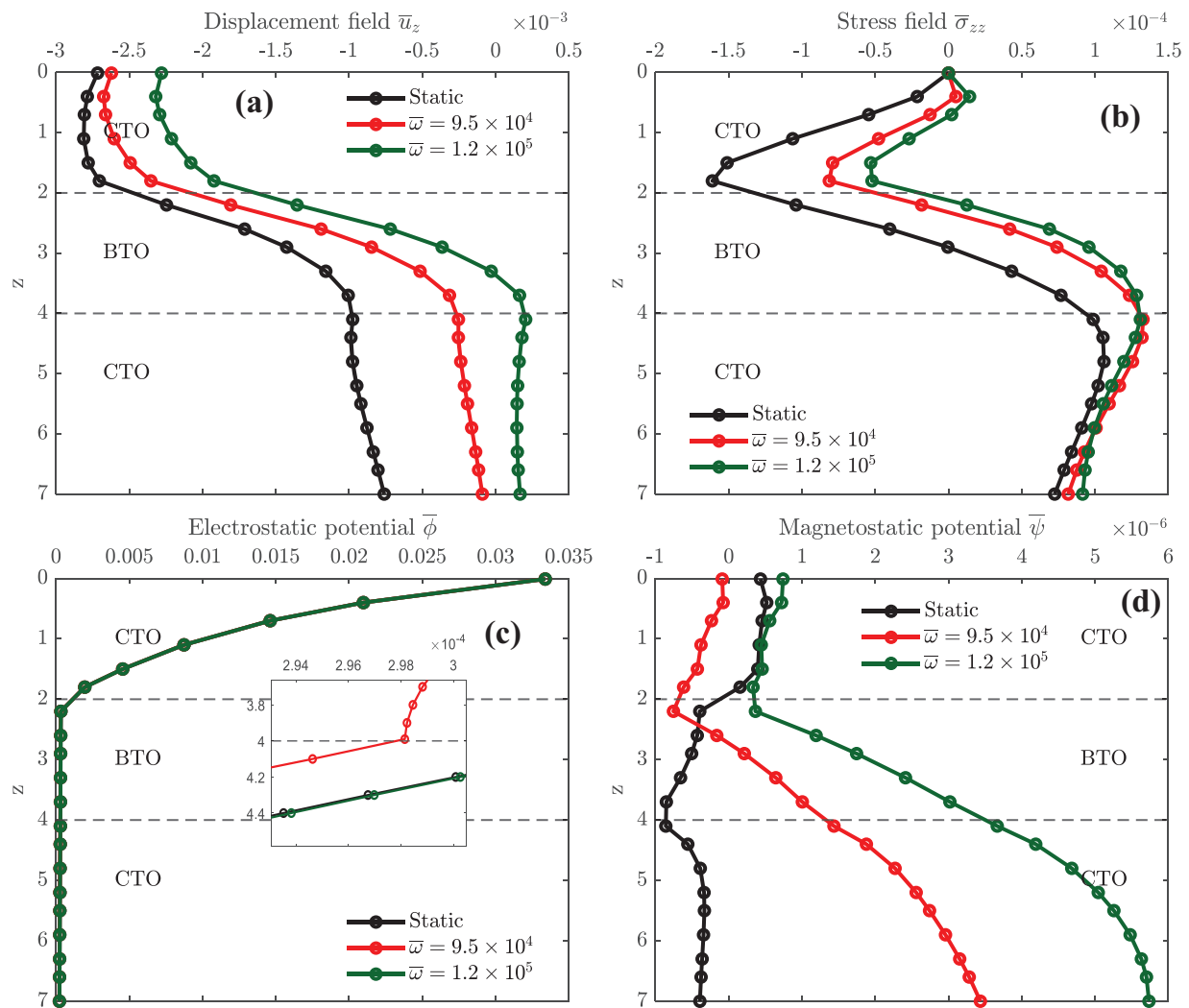
Figure 10: Effect of different frequencies on elastic displacement $\bar{u}_x$ in (a), stress $\bar{\sigma}_{zz}$ in (b), electrostatic potential $\bar{\phi}$ in (c), magnetostatic potential $\bar{\psi}$ in (d) in tri-layered CFO/BTO/CFO solid due to applied vertical electric displacement $\bar{d}_z$ on the surface

3.2.3 Under Horizontal Mechanical Loading

The static and time-harmonic responses of different layered structures subjected to circular horizontal mechanical load $\bar{p}_x$ are shown in Figs. 11–12.

Fig. 11 presents 2D contours of elastic displacement $\bar{u}_z$, magnetic potential $\bar{\psi}$, stress $\bar{\sigma}_{zz}$, and magnetic induction $\bar{B}_z$ induced by static horizontal mechanical load (i.e., $\bar{\omega} = 0$) in a homogeneous CFO half-space. Compared to Fig. 4 under vertical mechanical load, the field concentration is shifted to the edge of the loading circle instead of around its center. In other words, one should pay attention to the field variation near the edge when the half-space is under a horizontal mechanical load. Such insights are crucial for applications where understanding stress distribution and displacement patterns near loaded edges is essential for structural stability and performance assessment.
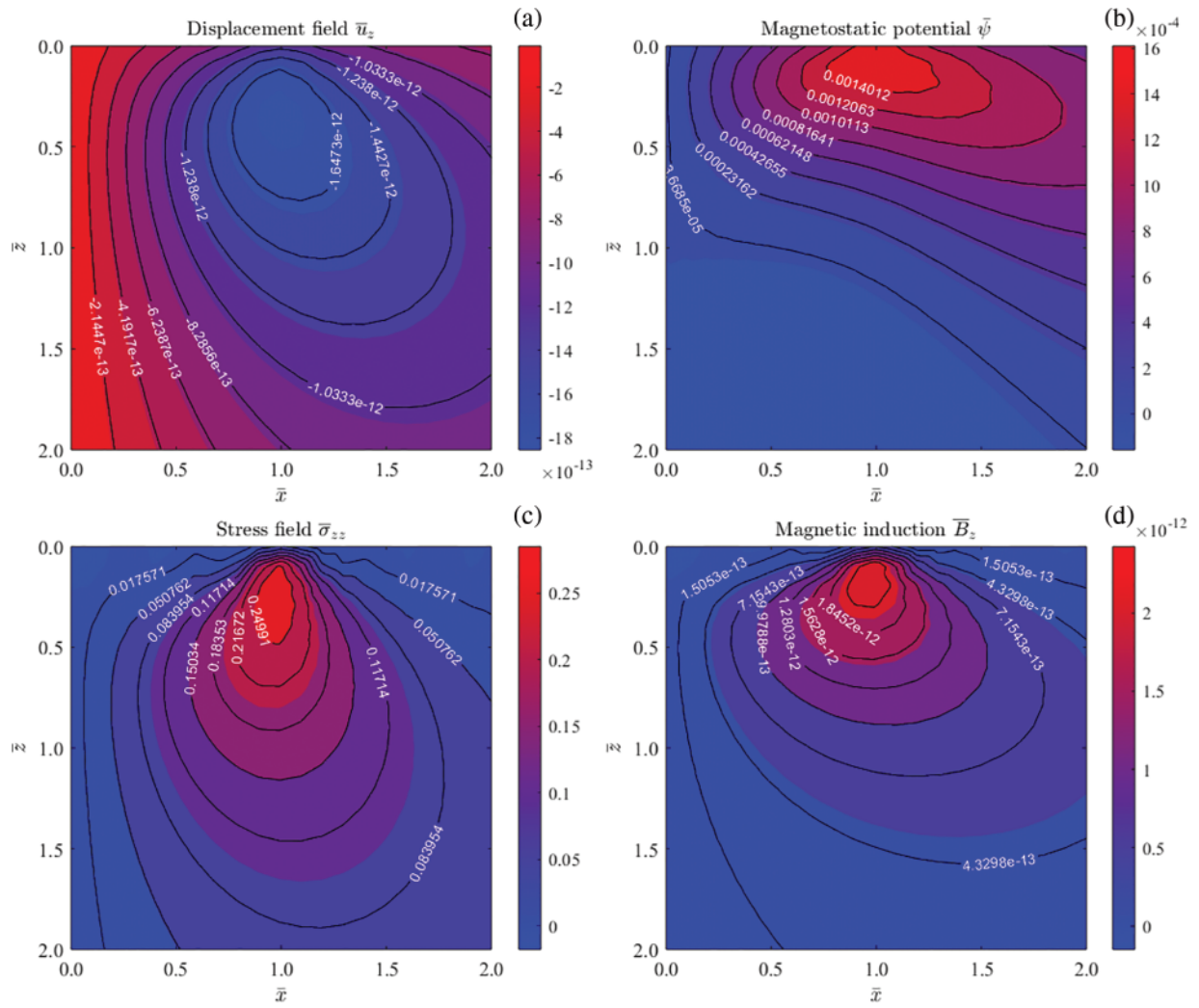
Figure 11: Contours of elastic displacement $\bar{u}_z$ in (a), magnetostatic potential $\bar{\psi}$ in (b), stress $\bar{\sigma}_{zz}$ in (c), and magnetic induction $\bar{B}_z$ in (d) in homogeneous CFO half-space due to applied horizontal mechanical load $\bar{p}_x$
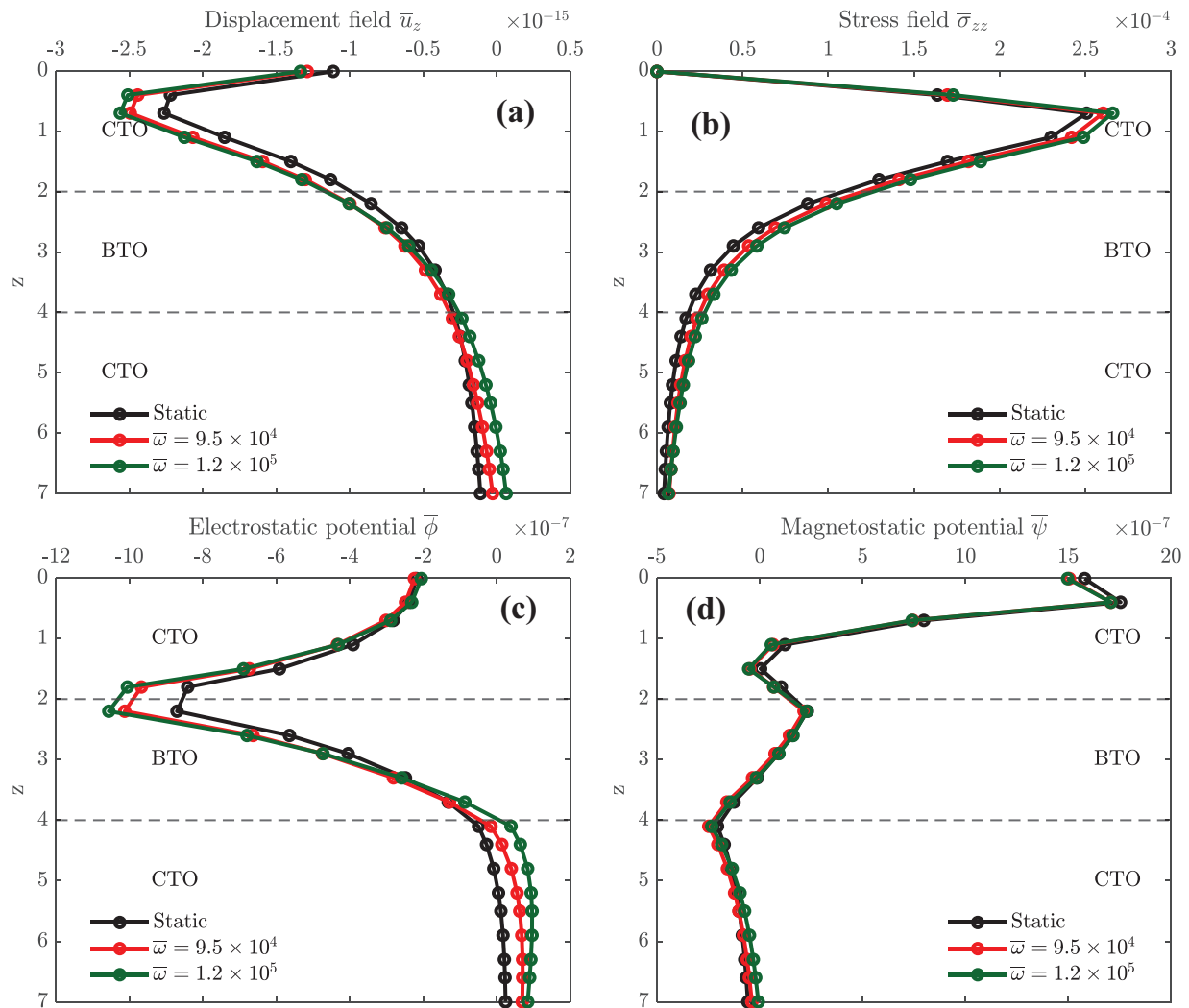
Figure 12: Effect of frequencies on elastic displacement $\bar{u}_x$ in (a), stress $\bar{\sigma}_{zz}$ in (b), electrostatic potential $\bar{\phi}$ in (c), and magnetostatic potential $\bar{\psi}$ in (d) in tri-layered CFO/BTO/CFO solid due to applied horizontal mechanical load $\bar{p}_x$

Fig. 12 presents the effect of different frequencies on elastic displacement $\bar{u}_z$, stress $\bar{\sigma}_{zz}$, electric potential $\bar{\phi}$, and magnetic potential $\bar{\psi}$ along $\bar{z}$-axis in tri-layered CFO/BTO/CFO half-space. It is observed that while both the elastic displacement and electric potential are different at different frequencies, particularly in the bottom CFO half-space, the stress and magnetic potential are relatively insensitive to frequency, a feature different from that observed in Fig. 7.

4 Conclusion

For a given multilayered MEE solid, we have derived the GFs due to surface (mechanical and electric) loads applied within a circle. The solution is in terms of the FBS along with the stable DVP matrix method for handling multiple layers. Since the involved coefficients are discrete Love numbers,

we can pre-calculate, save, and repeatedly use them later on. Numerical examples are carried out for layered structures made of $CoFe_2O_4$ and $BaTiO_3$, and the following features are observed:

1). Some physical quantities could be more sensitive to layering, while others not. For instance, under a vertical electric displacement on the surface, the electric potential is nearly independent of different layering structures, but other field quantities are completely different in different layering structures.

2). The primary physical quantities (displacements and electric/magnetic potentials) are more sensitive than others with frequency.

3). Field distributions in terms of contours are completely different under different (horizontal mechanical, vertical mechanical, and vertical electric) loads.

The results presented here provide valuable insights applicable across several domains. The contour plots illustrating elastic displacement, stress, electric potential, and magnetic potential under different mechanical and electric loads offer practical implications in advanced material science and engineering. Specifically, these findings are instrumental in the optimal design of different layered structures for enhancing mechanical and electromagnetic performance. Applications include the development of next-generation sensors capable of detecting subtle changes in stress and displacement, which are critical for structural health monitoring in civil infrastructure. In biomedical engineering, the ability to tailor material properties based on these findings supports the creation of biocompatible implants with improved durability and functionality. Moreover, in the realm of electromechanical systems, such as actuators and resonators, understanding frequency-dependent behaviors facilitates the design of more responsive and efficient devices for telecommunications and medical instrumentation.

While GFs lay out the significant insights and applications for the multilayered structure, there are limitations to this work that must be acknowledged. The key limitation of this work is the assumption of linear material behaviour, which may not accurately capture the complexities of real-world scenarios where nonlinear effects become significant. Future work should address this limitation by incorporating non-linearity into the material model.

Author Contributions: Sonal Nirwal: Writing—original draft, Visualization, Validation, Methodology, Investigation, Formal analysis. Ernian Pan: Writing—review & editing, Supervision, Software, Project administration, Methodology, Funding acquisition, Conceptualization. Chih-Ping Lin: Writing—review & editing, Supervision, Project administration, Methodology, Funding acquisition. Quoc Kinh Tran: Writing—review & editing. All authors reviewed the results and approved the final version of the manuscript.

Availability of Data and Materials: All data analyzed during this study are included in this published article.

Ethics Approval: Not applicable.

Conflicts of Interest: The authors declare that they have no conflicts of interest to report in the present study.

References

1. Spaggiari A, Castagnetti D, Golinelli N, Dragoni E, Scirè MG. Smart materials: properties, design and mechatronic applications. Proc Inst Mech Eng L: J Mater Des Appl. 2019;233(4):734–62. doi:10.1177/1464420716673671.

2. Barrett GR, Wolf N. High-rate, high-precision wing twist actuation for drone, missile, and munition flight control. Actuators. 2022;11(8):239. doi:10.3390/act11080239.

3. Sharma S, Kiran R, Azad P, Vaish R. A review of piezoelectric energy harvesting tiles: available designs and future perspective. Energy Convers Manag. 2022;254:115272. doi:10.1016/j.enconman.2022.115272.

4. Ganeson K, Tan XMC, Abdullah AAA, Ramakrishna S, Vigneswari S. Advantages and prospective implications of smart materials in tissue engineering: piezoelectric, shape memory, and hydrogels. Pharmaceutics. 2023;15(9):2356. doi:10.3390/pharmaceutics15092356.

5. Suchtelen SJ. Product properties: a new application of composite materials. Philips Res Rep. 1972;27:28–37.

6. Eerenstein W, Mathur ND, Scott JF. Multiferroic and magnetoelectric materials. Nature. 2006;442(7104):759–65.

7. Nan CW, Bichurin MI, Dong S, Viehland D, Srinivasan G. Multiferroic magnetoelectric composites: historical perspective, status, and future directions. J Appl Phys. 2008;103(3):031101–35.

8. Vinyas M. Computational analysis of smart magneto-electro-elastic materials and structures: review and classification. Arch Comput Methods Eng. 2021;28(3):1205–48.

9. Berlincourt DA, Curran DR, Jaffe H. Piezoelectric and piezomagnetic materials and their function in transducers. Phys Acoust: Principles Methods. 1964;1:202–4.

10. Kopyl S, Surmenev R, Surmeneva M, Fetisov Y, Kholkin A. Magnetoelectric effect: principles and applications in biology and medicine–a review. Mater Today Bio. 2021;12:100149.

11. Liu H, Lyu Z. Modeling of novel nanoscale mass sensor made of smart FG magneto-electro-elastic nanofilm integrated with graphene layers. Thin-Walled Struct. 2020;151:106749. doi:10.1016/j.tws.2020.106749.

12. Malleron K, Gensbittel A, Talleb H, Ren Z. Experimental study of magnetoelectric transducers for power supply of small biomedical devices. Microelectron J. 2019;88:184–9. doi:10.1016/j.mejo.2018.01.013.

13. Li M, Liu M, Zhou L. The static behaviors study of magneto-electro-elastic materials under hygrothermal environment with multi-physical cell-based smoothed finite element method. Compos Sci Technol. 2020;193:108130. doi:10.1016/j.compscitech.2020.108130.

14. Sasmal A, Arockiarajan A. Recent progress in flexible magnetoelectric composites and devices for next generation wearable electronics. Nano Energy. 2023;9:108733. doi:10.1016/j.nanoen.2023.108733.

15. Rojas-Díaz R, Sáez A, García-Sánchez F, Zhang C. Time-harmonic Green's functions for anisotropic magnetoelectroelasticity. Int J Solids Struct. 2008;45(1):144–58. doi:10.1016/j.ijsolstr.2007.07.024.

16. Pan E. Green's functions for geophysics: a review. Rep Prog Phys. 2019;82(10):106801. doi:10.1088/1361-6633/ab1877.

17. Özdemir Ö., Yücel H, Uçar YE, Erbaş B, Ege N. Green's functions for a layered high-contrast acoustic media. J Acoust Soc Am. 2022;151(6):3676–84. doi:10.1121/10.0011547.

18. Buroni FC, Sáez A. Three-dimensional Green's function and its derivative for materials with general anisotropic magneto-electro-elastic coupling. Proc R Soc A. 2010;466(2114):515–37. doi:10.1098/rspa.2009.0389.

19. Hwu C, Chen WR, Lo TH. Green's function of anisotropic elastic solids with piezoelectric or magneto-electro-elastic inclusions. Int J Fract. 2019;215:91–103. doi:10.1007/s10704-018-00338-6.

20. Moshtagh E, Eskandari-Ghadi M, Pan E. Time-harmonic dislocations in a multilayered transversely isotropic magneto-electro-elastic half-space. J Intell Mater Syst Struct. 2019;30(13):1932–50. doi:10.1177/1045389X19849286.

21. Yang ZX, Dang PF, Han QK, Jin ZH. Natural characteristics analysis of magneto-electro-elastic multilayered plate using analytical and finite element method. Compos Struct. 2018;185:411–20. doi:10.1016/j.compstruct.2017.11.031.

22. Xiao D, Han Q, Jiang T. Guided wave propagation in a multilayered magneto-electro-elastic plate: theoretical analysis and numerical simulations. J Intell Mater Syst Struct. 2016;27(10):1295–309.

23. Vattré A, Pan E. Semicoherent heterophase interfaces with core-spreading dislocation structures in magneto-electro-elastic multilayers under external surface loads. J Mech Phys Solids. 2019;124:929–56. doi:10.1016/j.jmps.2018.11.016.

24. Vattré A, Chiaruttini V. Singularity-free theory and adaptive finite element computations of arbitrarily-shaped dislocation loop dynamics in 3D heterogeneous material structures. J Mech Phys Solids. 2022;167:104954. doi:10.1016/j.jmps.2022.104954.

25. Hung PT, Phung-Van P, Thai CH. Small scale thermal analysis of piezoelectric-piezomagnetic FG microplates using modified strain gradient theory. Int J Mech Mater Des. 2023;19(4):739–61. doi:10.1007/s10999-023-09651-y.

26. Kiran MC. Thermal and hygrothermal buckling characteristics of porous magneto-electro-elastic skewed plates using third-order shear deformation theory. Mech Adv Mater Struct. 2023;1–16. doi:10.1080/15376494.2023.2227185.

27. Lyu Z, Ma M. Nonlinear dynamic modeling of geometrically imperfect magneto-electro-elastic nanobeam made of functionally graded material. Thin-Walled Struct. 2023;191:111004. doi:10.1016/j.tws.2023.111004.

28. Phung-Van P, Nguyen-Xuan H, Hung PT, Thai CH. Nonlinear isogeometric analysis of magneto-electro-elastic porous nanoplates. Appl Math Model. 2024;128:331–46. doi:10.1016/j.apm.2024.01.025.

29. Zhao X, Li XY, Li YH. Axisymmetric analytical solutions for a heterogeneous multi-ferroic circular plate subjected to electric loading. Mech Adv Mater Struct. 2018;25(10):795–804. doi:10.1080/15376494.2017.1308586.

30. Bui TQ, Hirose S, Zhang C, Rabczuk T, Wu CT, Saitoh T, et al. Extended isogeometric analysis for dynamic fracture in multiphase piezoelectric/piezomagnetic composites. Mech Mater. 2016;97:135–63. doi:10.1016/j.mechmat.2016.03.001.

31. Kiran R, Nguyen-Thanh N, Yu H, Zhou K. Adaptive isogeometric analysis-based phase-field modeling of interfacial fracture in piezoelectric composites. Eng Fract Mech. 2023;288:109181. doi:10.1016/j.engfracmech.2023.109181.

32. Manyo MJA, Ntamack GE, Azrar L. Time and frequency 3D-dynamic analyses of multilayered magnetoelectroelastic plates with imperfect interfaces. Arch Appl Mech. 2022;92(8):2273–301. doi:10.1007/s00419-022-02177-3.

33. Vaezi M, Shirbani MM, Hajnayeb A. Free vibration analysis of magneto-electro-elastic microbeams subjected to magneto-electric loads. Phys E Low-Dimens Syst Nanostruct. 2016;75:280–6. doi:10.1016/j.physe.2015.09.019.

34. Zhang XL, Chen XC, Yang E, Li HF, Liu JB, Li YH. Closed-form solutions for vibrations of a magneto-electro-elastic beam with variable cross section by means of Green's functions. J Intell Mater Syst Struct. 2019;30(1):82–99. doi:10.1177/1045389X18803456.

35. Zhao M, Zhang Q, Li X, Guo Y, Fan C, Lu C. An iterative approach for analysis of cracks with exact boundary conditions in finite magnetoelectroelastic solids. Smart Mater Struct. 2019;28(5):055025. doi:10.1088/1361-665X/ab0eb0.

36. Liu M, Gan Q. Experimental research on dynamic response of layered medium under impact load. Coatings. 2022;12(10):1474. doi:10.3390/coatings12101474.

37. Dong L, Closson AB, Jin C, Trase I, Chen Z, Zhang JX. Vibration-energy-harvesting system: transduction mechanisms, frequency tuning techniques, and biomechanical applications. Adv Mater Technol. 2019;4(10):1900177. doi:10.1002/admt.201900177.

38. Pan E, Lin CP, Zhou J. Fundamental solution of general time-harmonic loading over a transversely isotropic, elastic and layered half-space: an efficient and accurate approach. Eng Anal Bound Elem. 2021;132:309–20. doi:10.1016/j.enganabound.2021.08.006.

39. Love AEH. Some problems of geodynamics. Cambridge: Cambridge University Press; 1911.

40. Chu HJ, Zhang Y, Pan E, Han QK. Circular surface loading on a layered multiferroic half space. Smart Mater Struct. 2011;20(3):035020. doi:10.1088/0964-1726/20/3/035020.

41. Zhou J, Pan E, Lin CP. A novel method for calculating dislocation Green's functions and deformation in a transversely isotropic and layered elastic half-space. Eng Anal Bound Elem. 2023;152:22–44. doi:10.1016/j.enganabound.2023.03.022.

42. Qi S, Zhang P, Ren J, Ma W, Wang J. Precise solutions of dynamic problems in stratified transversely isotropic piezoelectric materials. Arch Appl Mech. 2023;93(6):2351–88. doi:10.1007/s00419-023-02386-4.